CHALMERS

Transport Properties of Bi_2Te_3 and Proximity Effect with Aluminum Superconductors

Master of Science Thesis in Nanoscale Science and Technology

Maria Ekström

Department of Microtechnology & Nanoscience
Division of Quantum Device Physics Laboratory
CHALMERS UNIVERSITY OF TECHNOLOGY
Göteborg, Sweden 2013

Transport Properties of Bi_2Te_3 and Proximity Effect with Aluminum Superconductors

Thesis for the degree Master of Science

MARIA EKSTRÖM

CHALMERS

Department of Microtechnology & Nanoscience
Quantum Device Physics Laboratory
Chalmers University of Technology
Gothenburg, Sweden 2012

Transport Properties of Bi_2Te_3 and Proximity Effect with Aluminum Superconductors
Thesis for the degree Master of Science in Nanotechnology
MARIA EKSTRÖM

Quantum Device Physics Laboratory
Department of Microtechnology & Nanoscience
Chalmers University of Technology
SE-412 96 Gothenburg, Sweden
Telephone:+46 (0)31 772 1000

Supervisor and examiner:
Prof. Floriana Lombardi

Cover: Description of cover figure

Printed at Chalmers Reproservice
Gothenburg, Sweden 2013

Transport Properties of Bi_2Te_3 and Proximity Effect with Aluminum Superconductors
MARIA EKSTRÖM
Department of Microtechnology & Nanoscience
CHALMERS UNIVERSITY OF TECHNOLOGY

Abstract

Topological insulators are materials with an insulating bulk and a gap-less metallic surface. On the surface the energy dispersion is linear and described by an odd number of Dirac cones. The interest for these materials was renewed recently when room temperature topological insulators among the bismuth compounds was discovered. Intensive research in the last years is focusing on observing the signatures of the topological surface. However, it is difficult to isolate from the bulk and the effects observed can have alternative interpretations. So far the surface states have not been totally distinguished from the bulk. Therefore topological insulators need further characterization and this thesis is a part of that research.

The two main focuses were to characterize the transport properties of molecular beam epitaxy grown Bi_2Te_3 thin films and Bi_2Se_3 single crystal with Hall effect and proximity effect. The Hall measurements of Bi_2Te_3 were used as feedback to the growers in collaboration to achieve better quality thin films. The Bi_2Te_3 showed negative charge carriers and the volume carrier concentration was improved from $1x10^{21}\,cm^3$ to $4.4x10^{18}\,cm^8$. The mobility was improved from $150\,^{cm^2}/_{Vs}$ to $5500\,^{cm^2}/_{Vs}$. For Bi_2Se_3 samples the typical values were 1.3 x $10^{19}\,cm^3$ and $5100\,^{cm^2}/_{Vs}$, which was comparable with the best Bi_2Te_3 films.

The properties of the topological insulators Bi_2Te_3 and Bi_2Se_3 were also investigated using proximity induced superconductivity in Josephson junctions and superconducting quantum interference devices with aluminum contacts at temperatures down to 20 mK. The Josephson coupling was confirmed by the response in microwave radiation and magnetic field. The height of the observed steps corresponded well to integer Shapiro steps. The response of the devices in magnetic field showed expected Fraunhofer patterns, where the effective areas for both the Josephson junctions and the superconducting quantum interference devices was in good agreement with the design. In addition the temperature dependence of the junctions was examined and evaluated in the clean and dirty regimes. The critical current scaled with the temperature, according to simulations of the resistively shunted junction model.

To further characterize the Bi_2Te_3 thin film topography and spectroscopy was measured, describing the roughness of the film and indicating a Dirac cone around 200 mV.

Acknowledgements

Here I will thank all the ones that have made this possible and the amazing opportunity to go to US . Structure - less personal to personal

Maria Ekström, Göteborg June 3, 2013

Contents

1

Introduction

A topological insulator is insulating in the bulk and has metallic states on the surface. Through the bulk insulator, the surface inherits its topological properties. As long as the bulk is insulating the surface states are protected and cannot change [1]. This is interesting for spintronics, quantum informatics and particle physics.

Topological insulators such as Bi_2Te_3 and Bi_2Se_3 are not newly discovered materials, but were used in the sixties as thermoelectric materials [3]. Almost fifty years later their interesting properties of high surface mobility made them candidates for quantum studies and devices.

1.1 Motivation and purpose

In addition to their high mobility of surface carriers, the topology of their surface states are protected by time-reversal symmetry [10]. The high stability of the surface states indicates that topological insulators could be useful in practical devices such as extremely high capacity interconnections [11].

The topological insulators' unique conductive properties could be useful in electronic devices. Because of their stability and the fact that they allow simple manipulation of the spin [12], they could be used for magnetic storage in hard drives replacing the microprocessor [11].

In the interfaces between superconductors and topological insulators, local Majorana excitations are predicted [13]. Majorana particles were discovered in particle physics and are their own antiparticles [1]. An observation of a Majorana particle would be a step towards a future of quantum computing with topological phases.

Topological insulator materials are many and there are 2D and 3D types, which means that they have 1D and 2D surface states [2]. In this project 3D topological insulators will be discussed and it will focus on the second generation of 3D topological insulators; Bi_2Te_3 and Bi_2Se_3.

Both Bi_2Te_3 and Bi_2Se_3 are topological insulators with simple surface states in comparison to other TIs [1]. The surface states are non-degenerate and the electron dispersion is almost an idealized Dirac cone [10] in these compounds.

Bi_2Te_3 and Bi_2Se_3 have relative large bulk band gap and should in principle keep their topological behavior up to higher temperatures than other topological insulators [14, 15]. This indicates that their topological behavior might be seen at room temperature, giving Bi_2Te_3 and Bi_2Se_3 great potential for usage in applications.

Even though Bi_2Te_3 and Bi_2Se_3 have promising properties, there are still difficulties to see the surface states in realizations. The materials have impurities and vacancies in the bulk. This leads to a bulk conduction, screening the signature of the surface.

The purpose of this project is to investigate the properties of Bi_2Te_3 and Bi_2Se_3. To characterize the materials the main tasks are to fabricate devices and measure Hall effect and proximity effect with an aluminum superconductor. The results will be compared to previous research and theoretical predictions. It will further improve the knowledge of these strange materials and be useful for continuing research and future applications.

1.2 Problem description

The samples will be fabricated on-chip in the MC2 cleanroom. To get flakes from Bi_2Te_3 and Bi_2Se_3 two methods will be used; exfoliation and direct patterning on top of the topological insulators. The flakes will be connected to devices using either electron beam lithography or photolithography, together with evaporation of an aluminum superconductor.

Firstly Bi_2Te_3 and Bi_2Se_3 will be characterized by measurements of Hall effect, hoping for fractional quantum Hall effect. The films will be characterized to obtain its carrier concentration, mobility and thickness. Through the results of the Bi_2Te_3 thin films, the growth process will be optimized to get less defects in the films.

The Hall effect measurements will be conducted from room temperature down to two kelvin. From the films with low carrier concentration and high mobility, further characterizations will be done. The topological surface state will be characterized by measuring the Josephson effect through superconductor - topological interfaces and in superconducting quantum interference devices. The Josephson effect will depend on the superconductor used and will therefore be measured in sub-kelvin temperatures.

In addition to the transport measurements, the surface of Bi_2Te_3 will be characterized in a scanning tunneling microscope through topography and spectroscopy measurements.

1.3 Reading instructions

This sections describes the outline of the report, with the intention to guide the readers through the thesis. The reader is assumed to have knowledge about superconductivity theory and some knowledge about cleanroom fabrication. In the second chapter a theoretical description of topological insulators and their crystalline structure is given. It further discusses about the physics used for observation of Hall effect and Josephson effect.

The experimental realization is described in chapter three and four. In chapter three the chip design is explained in detail. Chapter four covers methods and technologies used during the cleanroom fabrication. This is followed by measurements in chapter five, which describes the sub-Kelvin measurement technique and the electronics used.

The results are presented and discussed in chapter six. These results includes current-voltage measurements from Hall measurements, magnetic patterns and temperature dependence measurements. The results and discussions are concluded in chapter seven. The Appendix has further information about fabricated samples and technical information.

2

Theory

Topological insulators differs from conventional insulators since they have metallic states on the surface of their insulating bulk. These metallic states inherits their topological properties from the bulk insulator and are protected from change as long as the bulk is insulating [1]. This is commonly known as a topological knot and describes the topological insulators electronic wave function through momentum space.

When a topological insulator is connected to a superconductor, the superconductivity is bound by the topology and is protected against non-magnetic disturbance. Using superconductivity or Hall effect topological insulators can be characterized, which be described later in this chapter. This chapter will also present the Majorana particle, a particle that should appear at interfaces between topological insulators and superconductors. But first the main topic of this thesis; topological insulators, will be explained.

2.1 3D Topological insulators

In a normal insulator the valence band and conduction band are separated by a well defined energy gap. This gap is much larger in an insulator than in a semiconductor and the Fermi level lies between the minimum of the conduction band and the maximum of the valence band.

In a 3D topological insulator the Fermi level lies within the bulk band gap, however there are also surface states with a different energy dispersion. The bulk energy dispersion is similar to a normal insulator. They are doubly degenerated modes separated with a gap, as illustrated with blue lines in Figure 2.1 [16]. In the figure there are also a pair of red dotted lines. These are a pair of non-degenerated lin-

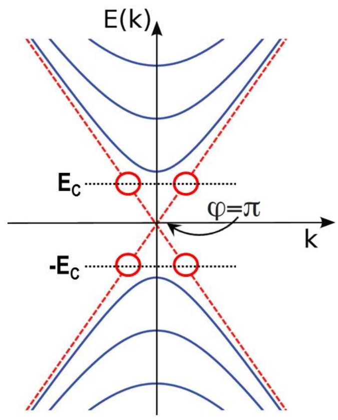

Figure 2.1: The energy levels of a 3D topological insulator, where the normal insulator valence and conduction bands are illustrated in blue. The additional linearly dispersed cone showed with red dotted lines, originates from the surface state [9, 16].

early dispersed gapless modes, which originates from the surface and are the so called surface states.

2.1.1 Crystal structure of Bi_2Te_3 and Bi_2Se_3

The 3D topolocial insulators Bi_2Te_3 and Bi_2Se_3 have rhombohedral structure and one unit cell consists of five atoms. In Figure 2.2 the crystalline structure is shown [14, 17].

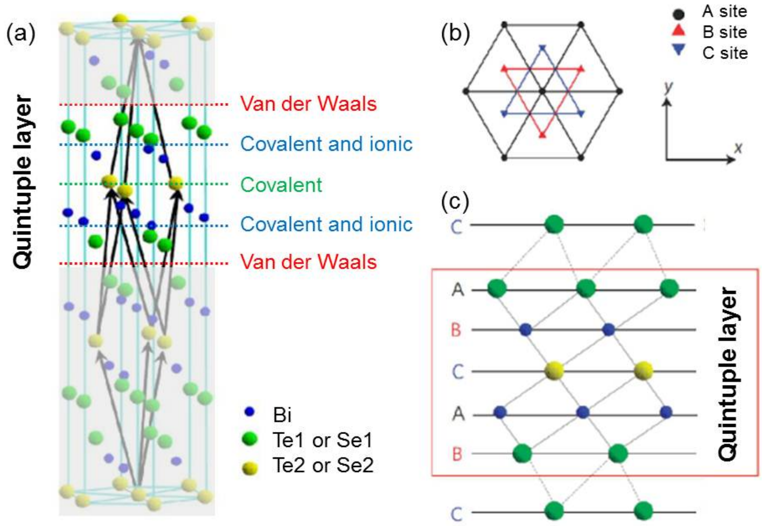

Figure 2.2: (a) The crystalline structure of Bi_2Te_3 and Bi_2Se_3 and (b) the top view. (c) The fifteen layered hexagonal supercell is divided into a basic unit cell with five atomic layers. Between these basic unit cells van der Waals interaction takes place [14, 18].

These topological insulators have layered structure which can be divided into a fifteen layered hexagonal supercell or a basic cell with five atomic layers, a quintuple layer. Within the quintuple layer the bonding is strong, dominantly covalent and partly ionic. Between the quintuple layers van der Waals interaction is the main interaction, hence much weaker. Consequently, a favored cleavage plane exists between the quintuple layers [14, 17, 19].

The spin-orbit coupling in Bi_2Se_3 and Bi_2Te_3 is large enough to twist the band structure [20]. A model explaining this is described in Appendix B.2. This twist or cross over of conduction and valence band forms a Dirac cone on the surface [14], which is seen as the red dotted lines in Figure 2.1. If the bands cross over an odd number of times, there is an odd number of Dirac cones on the surface. This is the case for topological insulators, like Bi_2Te_3 and Bi_2Se_3.

2.1.2 Topological invariance and stability of the state

Different structures with energy bandgaps can be classified as equivivalent classes of the Bloch Hamiltonian if they can be continiously deformed into each other without closing the band gap[1].

A way to express topology is the mapping of the Brillouin zone onto the unit sphere [21]. This means that we map the energy levels in momentum space starting with $k = 0$

to one pole of the unit sphere and continue until $k = \pi$. The trajectory on the sphere can then end up with $k = \pi$ on the same pole or the opposite. These trajectories are topologically distinct. The Dirac cones described in the previous section are in more than one dimension and the mapping covers an area of the sphere instead of a trajectory. In the trivial phase, i.e. non-topological phase, the sphere is covered and then uncovered while mapping. In the topological phase the odd number of Dirac cones covers the sphere an odd number of time, and the result is a covered unit sphere. This type of topological invariance is called winding invariant [21].

A way to think about the winding invariance is the number and direction of a rubber band around a cylinder, shown in Figure 2.3. The rubber band can be put in mathematically positive or negative direction around the cylinder, which leads to either a positive or negative ± 1 winding number. The cylinder is infinitely long and the rubber band cannot be taken off. It can be twisted and deformed, but the overall direction and number of laps around the cylinder stays the same. The rubber band can also be twisted two times around the cylinder without crossing itself, as to the right in Figure 2.3. The total number of laps with direction is zero, since the positive and negative compensate. The rubber band can also be taken off the cylinder. This is the topological class zero, in which both vacuum and conventional insulators belong.

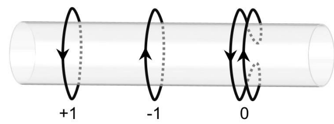

Figure 2.3: The winding invariance can be illustrated as the number and direction of a rubber band around a cylinder.

2.1.3 Topological superconductor

The topological twist in the topological insulators is protected by quasiparticle parity conservation [20] and the topological invariance [21]. When a topological insulator is used as the weak link between two superconductors, as shown in 2.4(a), the superconducting order will therefore be protected against non-magnetic disorder. In the figure the zero energy edge state lays within the superconducting gap and this is the surface state of the topological insulator. Cooper pairs transfer from one superconductor to the other, crossing the topological insulator at zero energy. However, this can only happen if the phase difference between the superconductors is π [9].

If the topological insulator is doped or not ideal the energy diagram shifts in energy. In Figure 2.4(b) the topological insulator is doped, shifting the energy levels down in energy in comparison to the superconductors. When the conduction band lays below the superconducting gap, Cooper pairs can tunnel through the conduction band i.e. the bulk of the topological insulator. The conduction through the bulk is characterized by a metallic behavior and screens the detection of surface effects.

Therefore one of the constraints to observe the zero modes in 3D topological insulator systems is that the chemical potential needs to lay within the bulk band gap. It seems that this can be established experimentally [16], but that the key difficulty still is to distinguish the conduction through the surface from the bulk. As a consequence the bulk of Bi_2Se_3 and Bi_2Te_3 needs to be insulating enough, which means have a low carrier concentration while a relatively high mobility. This can be characterized by Hall measurements, described in the next section.

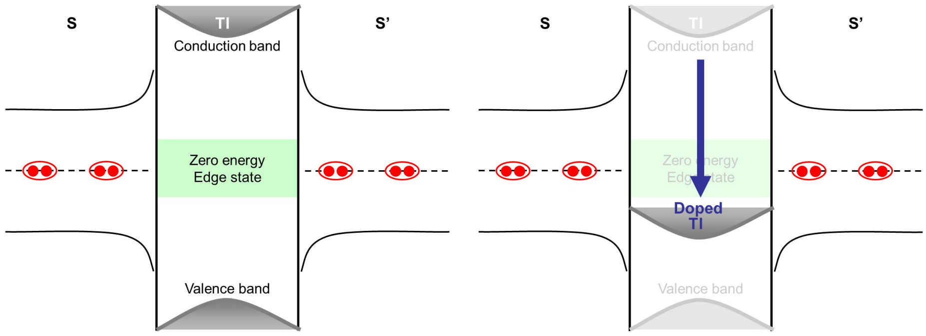

(a) Josephson junction with TI (b) Doped TI

Figure 2.4: The energy diagram of two superconductors in a Josephson junction with a topological insulator as the weak link. (a) The ideal state of the system is shown. The Cooper pairs (two red electrons paired up) in the superconductors S and S', have to tunnel through the surface state of the topological insulator. (b) When the topological insulator is doped or is subjected to defects, the energy levels can shift. If the bulk conduction band of the topological insulators is below the superconducting gap the Cooper pairs can tunnel through the bulk and the weak link behaves like a metal.

2.2 Hall effect

The Hall effect describes the conductance of charge carriers in the presence of a magnetic field. It can be seen when measuring the voltage transverse to an electric current through a conductor. Without a magnetic field the net charge moves, following an almost straight path and the transverse voltage is zero. When applying a perpendicular magnetic field the trajectory becomes curved. This results in a separation of the oppositely charged particles perpendicular to both the magnetic field and the current direction. The charge separation give rise to an electric field, which prevent further migration of the charge. A steady electrical potential is then established [22] resulting in a non-zero transverse voltage.

Assuming one type of charged carriers, the Hall voltage and the Hall coefficient are defined as

$$\begin{cases} V_H = -\dfrac{IB}{net} \\ R_H = \dfrac{E_y}{\rho_x B} = \dfrac{V_H t}{IB} = \dfrac{1}{nq} \end{cases} \tag{2.1}$$

where I is the applied current and B is the perpendicularly applied magnetic field (z-direction). The thickness of the material is expressed as t, the charge carrier concentration as q and the charge carrier concentration as n. The current density of the charge carriers is written as ρ and the induced electric field as E_y.

When the charge carriers are negative the Hall coefficient, R_H, is negative [22]. Accordingly the type of charge carriers can be investigated by Hall measurements.

In Hall measurements the charge carrier mobility can be obtained from the longitudinal conductance σ at zero field and the Hall coefficient from eq 2.1 as

$$\mu = \frac{\sigma}{nq} = \sigma R_H = \frac{\sigma V_H t}{IB}. \tag{2.2}$$

The mobility describes how easily the charge carriers move through the material under an electric field.

2.2.1 Quantum Hall effect

In a two dimensional electron gas system a modified effect can be observed, the quantum Hall effect. It occurs at low temperature when a strong magnetic field is applied to a semiconductor. Due to the magnetic field the electrons move in cyclotron orbits, which are quantized with discrete energy levels, known as Landau levels. The magnetic field puts the Fermi energy below the magnetic energy and above the kinetic energy [23]. Depending on the magnetic energy the Landau levels cross the Fermi energy one by one and results in a quantized behavior of the Hall effect [24].

In a regular conductor, the electrons are allowed to move backwards and forwards. In the quantum Hall state these degrees of freedom are spatially separated as an upper and lower edge state. Since the states are separated, scattering cannot mix the backward and forward electrons. This means that the electrons will move around impurities without scattering and that the edge states are stable [18].

Similarly to the Hall effect, the quantum Hall effect is not geometry dependent. Thus, the effect does only depend on the topology of the state [18].

2.2.2 Shubnikov-de Haas effect

As mentioned above a strong magnetic field is required to observe the quantum Hall effect. This is due to the discrete quantized orbits of the electrons. When the magnetic field is weaker the spacing between these levels is smaller and an intermediate state between the quantum Hall state and the Hall state can occur.

This intermediate behaviour is called the Shubnikov-de Haas effect and is described by the oscillations of the longitudinal (to current) resitivity with the magnetic field. They also originate from the Landau quantization. The oscillations occur when

$$\begin{cases} E_F > \hbar\omega_c > k_B T \\ \omega_c \tau > 1 \end{cases}, \omega_c = \frac{eH}{cm^\star} \tag{2.3}$$

where ω_c is the cyklotron frequency, τ is the lifetime and $m^\star$ is the effective mass. This means that in contrast to the quantum Hall state the Fermi energy has to be above the magnetic energy to enable observation of the Shubnikov-de Haas oscillations [22].

The magnetic field causes the electrons to move in cyclotronic motions. Therefore the electrons' energies will then vary in respect to the Fermi surface. These variations will result in an oscillating conductance.

2.3 Josephson junctions

A Josephson junction can be constructed by two superconducting electrodes weakly coupled An example can is shown in Figure 2.5. A superconductor can be described with a complex order parameter, $\Psi = \rho e^{i\theta}$. The order parameter describes the macroscopic wave functions of the Cooper pairs with the phase θ and the density $\rho = |\Psi|^2$.

The Cooper pairs can tunnel through the barrier if the wave function of the two superconductors overlap. The tunneling Cooper pairs results in a current through the

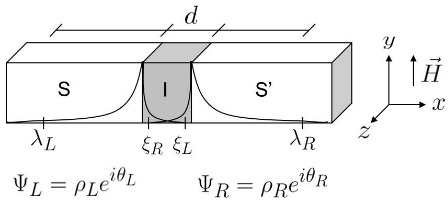

Figure 2.5: Two superconductors coupled through an insulating barrier.Each superconductor can be described by a wave function Ψ and a phase θ. The wave function leaks into the insulating barrier, within a distance called the coherence length ξ. If the wave functions of the two superconductors overlap in the barrier, the Cooper pairs can flow from one superconductor to the other.

Josephson junction which depends on the phase difference, $\phi = \theta_R - \theta_L$, between the wave functions on each side of the junction. This effect is described by the DC and AC Josephson equations;

$$\begin{cases} I_J = I_c \sin\phi \\ V_J = \dfrac{\hbar\dot{\phi}}{2e}. \end{cases} \tag{2.4}$$

The first equation describes that the phase difference across the junction depends on the bias current. A current can flow without resistance up to a specific value of the current I_c, which is the temperature dependent critical current. This is known as the DC Josephson effect. When the current exceeds this value the voltage switches from zero to a finite value due to resistive quasiparticle tunneling. The second equation describes the AC Josephson effect where a voltage over the junction changes the phase difference in time. If a constant nonzero voltage is applied over the junction the phase will increase with time as $\phi = \phi_0 + \frac{2eV}{\hbar}t$ and the current density will change to

$$J = J_c \sin\left(\phi_0 + \frac{2eV}{\hbar}t\right) \tag{2.5}$$

where $\omega_0 = 2eV/\hbar$ represents the Josephson frequency [25].

2.3.1 Response to magnetic field

A way to study a Josephson junction is to apply an external magnetic field $\vec{H} = H_y\vec{y}$ perpendicular to the junction area in Figure 2.5. Assuming electrodes are much thicker than the London penetration depth, the phase difference between two spacial points depends on the magnetic field as

$$\frac{\partial\phi}{\partial x} = \frac{2e}{\hbar c}d'H_y. \tag{2.6}$$

The effective thickness of the barrier, $d' = \lambda_L + \lambda_R + d$, is the London penetration depths in the electrodes added to the true barrier thickness. Inserting the solution into the Josephson relations, the current density is spatially modulated by the magnetic field. Therefore the critical current will be geometry dependent. In the simplest case the junction is rectangular with an uniform zero field current distribution.

Then the critical current will depend on the applied perpendicular magnetic field as

$$I_c(H) = I_c(H=0)\left|\frac{\sin \pi \frac{\Phi}{\Phi_0}}{\pi \frac{\Phi}{\Phi_0}}\right| \qquad (2.7)$$

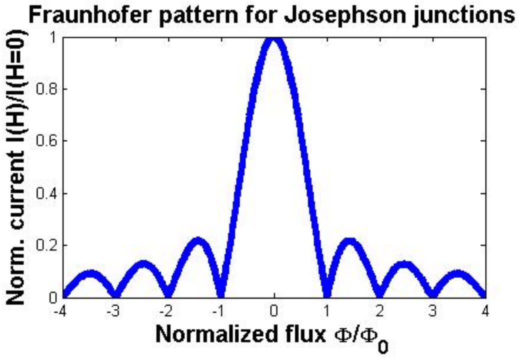

Figure 2.6: The expected Fraunhofer pattern from equation 2.7. The maximas decay exponentially with the magnetic field.

where Φ is the magnetic flux through the junction defined as $d\Phi = \vec{H} \cdot d\vec{S}$ and $\Phi_0 = \frac{h}{2e}$ is the magnetic flux quantum. This behavior of the critical current is oscillatory and has the form of a Fraunhofer diffraction pattern seen in figure 2.6. In absence of a magnetic field, the critical current is maximal but decays exponentially when increasing the magnetic field. If the junction is less uniform the critical current decays slower than exponentially [9]. When the magnetic flux is a multiple of the flux quantum, the critical current is zero appearing as minimums in the Fraunhofer pattern.

2.3.2 Response to microwave irradiation

In addition to magnetic field manipulation, the Josephson junctions also respond to microwave radiation. The simplest case for an applied voltage is when $V = V_0 + V_1 \cos \omega_1 t$, a combined DC and AC voltage. Using this voltage in the voltage Josephson relation in equation 2.4 and integrate over time, the phase difference over the junction will be

$$\phi = \phi_0 + \omega_0 t + \frac{2eV_1}{\hbar\omega_1}\sin \omega_1 t. \qquad (2.8)$$

The first term describes the DC Josephson phase difference as in equation 2.4. The second term originates from the DC applied voltage with $\omega_0 = \frac{2eV_0}{\hbar}$. The phase variation from the AC voltage is described by the third term. This results in AC supercurrents at the Josephson frequency but also at side frequencies determined by the third term.

Evaluating the relation 2.8 for the phase difference in the AC Jospehson equation 2.5, the current is described as a sine of the sine function. This can be expressed in terms of Bessel functions and results in

$$I = I_c \sum_n (-1)^n \mathrm{J}_n\left(\frac{2eV}{\hbar\omega_1}\right)\sin(\phi_0 + \omega_0 t - n\omega_1 t) \qquad (2.9)$$

where J_n is the n^{th} Bessel function.

The response will appear as steps in the current-voltage characteristics. The steps will appear at constant voltages when $V_n = \frac{n\hbar}{2e}\omega_1$ where n is an integer and ω_1 the angular frequency of the applied microwave radiation. The height of the steps is given by

$$I_n = 2I_c \mathrm{J}_n\left(\frac{2eV}{\hbar\omega_1}\right). \qquad (2.10)$$

and are determined by both the amplitude and frequency of the applied voltage signal. These steps are named after Shapiro, who first observed the effect in 1963 [26].

The applied voltage at microwave frequencies requires a system impedance of a few Ohms, but most systems use transmission lines with the characteristic impedance of $50\,\Omega$ [26]. Therefore a current source is more commonly used. The analysis is more complicated, but the effect is the same and results in steps in the current-voltage characteristics.

2.3.3 Resistively shunted junction model

For finite voltage, the resistively shunted junction model, RSJ, can be used to describe the behavior of a Josephson junction. In this model a Josephson junction is shunted by a resistance R and a capacitance C, as can be seen in Figure 2.7. The resistance relates to the dissipation in the finite voltage regime and is depending on the voltage. It is usually assumed to be constant and equal to the normal tunneling resistance R_N. The capacitance reflects geometric shunting capacitance between the two electrodes. It depends on the area of the junction in relation to the barrier thickness.

Assuming current bias and no thermal fluctuations, the total junction current of the circuit in figure 2.7 is

$$I = \frac{V}{R} + C\frac{dV}{dt} + I_c \sin\phi. \tag{2.11}$$

Using the Josephson voltage relation from equation 2.4, the expression for the total current can be written as

$$I = \frac{\hbar}{2eR}\dot{\phi} + C\frac{\hbar}{2e}\ddot{\phi} + I_c \sin\phi. \tag{2.12}$$

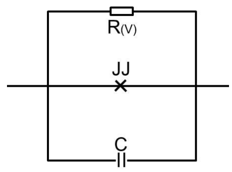

Figure 2.7: In the RSJ model, the Josephson junction can be described by the ideal Josephson junction, JJ, in parallel with the resistive effects, R(v), and the capacitative, C. Depending on the size of the capacitance different approximations can be applied.

However, in real systems thermal fluctuations are present. These can be accounted for by adding a time dependent noise term to the current relation and describes the noise due to a resistive flow of quasiparticles [25]. The noise term is not added to the Josephson voltage relation since the equation is not dissipative. The noise term is statistical and the equations can no longer be treated as functions of time, but as probabilities. The measurable quantities are averages.

The junction area can be considered small when the distance between the electrodes (d in Figure 2.5) and the thickness of the barrier (y-direction in Figure 2.5) is smaller than the width of the electrodes (z-direction in Figure 2.5). When the junction area is small, the capacitance C is negligible and the junction can be assumed to be overdamped. This means that the motion of the particles is negligible in comparison to the force acting on them. Using these approximations simulations of the current-voltage characteristics was done for different temperatures and can be seen in Figure 2.8.

The current-voltage characteristics in Figure 2.8 are rounded in comparison to the current-voltage at zero temperature. At temperatures above zero, the thermal fluctuations softens the ideally sharp jump and the jump appears at currents lower than the true critical current. When the temperature is higher the current-voltage characteristics are almost linear, i.e. $V \to IR_N$. At low temperatures, the thermal fluctuations are absent. Then the Josephson junction behaves as an ideal Josephson junction with a jump from zero voltage to a finite voltage at $I = I_c$ as describe in Section 2.3. Above

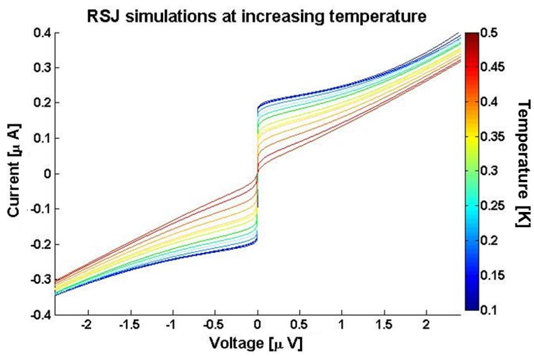

Figure 2.8: RSJ simulations of IV characteristics for an overdamped Josephson junction. The curves approaches the step function at lower temperature with an increasing well-defined critical current.

the critical current the tunneling through the junction is due to quasiparticles and the current-voltage characteristics are resistive.

2.4 Superconducting quantum interference devices

A superconducting quantum interference device, SQUID, is a superconducting loop with two Josephson junctions in parallel as in Figure 2.9. It is a very sensitive flux sensor and can be seen as a flux to voltage converter.

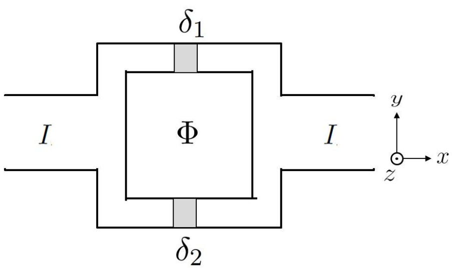

Figure 2.9: Two Josephson junctions in parallel in a superconducting loop constructs a SQUID. When a current is driven through the loop the phase differences through the two Josephson junctions are δ_1 respective δ_2 and the flux through the loop is Φ.

The London equations relate currents to electromagnetic fields in and around superconductors [27], with the superconducting phase θ and the supercurrent $\vec{J}_s$. From the derivation of the London equations, the phase gradient $\nabla\theta$ is given by the expression

$$\begin{aligned} -\Lambda\vec{J}_s &= \frac{\hbar}{2e}\nabla\theta + \vec{A} \text{ , with the London constant} \\ \Lambda &= \frac{m}{2n_p e^2} \end{aligned} \tag{2.13}$$

where $\vec{A}$ is the electromagnetic vector potential from an applied magnetic field and n_p is the number of Cooper pairs. The equation can be integrated over a closed loop inside the superconductors where the screening current is zero. Therefore

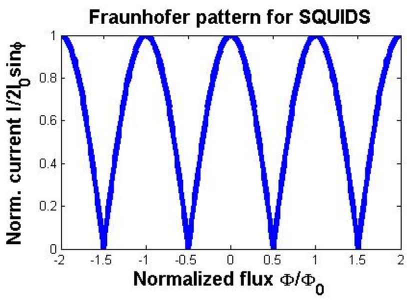

Figure 2.10: The expected Fraunhofer pattern from equation 2.16. In contrast to the exponentially decaying pattern for Josephson junctions in figure 2.6, the value of the maximas does not change with the magnetic field.

$$-\Lambda \oint \underbrace{\vec{J}_s}_{=0} d\vec{l} = \frac{\hbar}{2e} \underbrace{\oint \nabla\theta d\vec{l}}_{=2\pi n-\delta_1+\delta_2} + \oint \vec{A} d\vec{l} \tag{2.14}$$

where the phase differences through the two Josephson junction are δ_1 and δ_2 respectively.

The third term can be rewritten with Stokes' theorem as $\oint \vec{A} d\vec{l} = \int \nabla \times \vec{A} d\vec{S} = \int H d\vec{S} = \Phi$, where Φ is the total magnetic flux through the SQUID. Introducing the flux quanta $\Phi_0 = \frac{h}{2e}$, equation 2.14 can be rewritten as

$$\delta_1 - \delta_2 = 2\pi n + 2\pi \frac{\Phi}{\Phi_0}. \tag{2.15}$$

The flux Φ sweeps over a full range of n and this term does therefore not contribute to the total current. Further assuming two identical Josephson junctions, the total current through the SQUID is

$$I_{TOT} = I_0(\sin\delta_1 + \sin\delta_2) = 2I_0 \sin\varphi \left|\cos\frac{\delta_1 - \delta_2}{2}\right| = 2I_0 \sin\varphi \left|\cos\frac{\pi\Phi}{\Phi_0}\right| \tag{2.16}$$

with $\varphi = \frac{\delta_1+\delta_2}{2}$. The Fraunhofer pattern for a SQUID is shown in 2.10 and differs from the Josephson junction pattern in figure 2.6. In contrast to the exponentially decaying pattern from the Josephson junctions, the maximas in the SQUID pattern are constant. The current maximas in the SQUID occurs when the magnetic flux through the loop is a multiple of the flux quantum. Then the phase difference between the two Josephson junction is a multiple of π.

2.5 Majorana excitations

When a topological insulator is used as the barrier in Josephson junctions and SQUIDs, Majorana particles can emerge as zero modes at the interfaces between the topological insulator and the superconductors. Majorana particles are non-abelian anyons and their own anti-particles. In the non-abelian statistics the ground state is degenerated and separated from the excited states by a gap [28]. Under these special conditions an ordinary fermion can be composed of two Majorana particles [29].

To be able to measure the signatures of a Majorana particle and not just the ordinary fermion, a single Majorana particle has to be spatially separated from the other. Otherwise, it will pair up with another Majorana particle and appear as an ordinary fermion. A model to understand this was proposed by Kitaev [30] with a one dimensional quantum wire subjected to p-wave superconductive pairing. The quantum wire can be described by a tight-binding chain, where the spinless electrons are hopping between the sites in the chain.

Each electron in the chain can be seen as a composition of two Majorana particles as in Figure B.1. In the Kitaev chain the Majorana particles can pair up in two ways; with the other Majorana particle in same site of the chain or with another Majorana particle in a neighboring site. When the Majorana particles pairs up in the same site they are bound together and form ordinary fermions, in this case electrons. If the Majorana particles pair with particles in neighboring sites, this leaves two unpaired Majorana particles in both ends of the chain. These are spatially separated. The later pairing describes the topological superconductor phase [30].

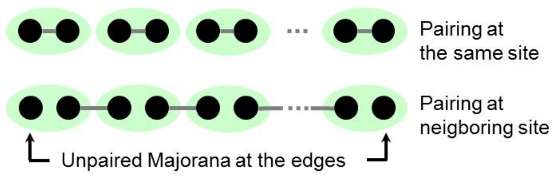

Figure 2.11: The Kitaev chain describes two ways that the Majorana particles can pair up. In the upper chain Majorana particles in the same site pair up, bounding them to normal fermions. In the lower chain the Majorana particles pair up with another Majorana particle in a neighboring site. This leaves two unpaired spatially separated Majorana particles at the two ends of the chain, describing the topological superconductor phase.

So far the Majorana particles have not been isolated, however signatures of Majorana particles have been reported [31]. In topological-Josephson junctions an additional conductance peak at zero bias was observed [16], but the peak is predicted to be quantized in presence of the Majorana zero mode and this has not been observed. Moreover, theoretical perturbation simulations predicts a 4π- periodicity of the tunneling current in SQUIDs [32] instead of the normal case of 2π [20]. This is due to the allowance of single-electron tunneling through the Majorana zero modes, but the effect could also be induced in the SQUIDs by flux trapping.

3

Design

TO CHARACTERIZE THE TOPOLIGICAL INSULATORS, two different approached was used. The Bi_2Te_3 growth and the Bi_2Se_3 crystals were first characterized with Hall measurements. A sample with low carrier concentration and high mobility demonstrate a topological insulator with few defects. This gave the best chance of observing surface conduction and the surface signature of the topological insulator.

Some of the samples with the lowest carrier concentration and the highest mobility were chosen for further characterization by inducing superconductivity. In this design there were two main types of circuit elements; SQUIDs and Josephson junctions. There were also two different fabrication approaches. One where the fabrication was done directly on the film and one where the topological insulator elements were achieved by exfoliation. The latter technique was initially used and the layout on the chip was varying for each sample since the exfoliation technique distributed the flakes in a random fashion. This chapter will therefore only discuss the circuit elements and not show the full layout. The fabrication of the circuit elements will be discuss in the next chapter.

Another way to induce superconductivity into the topological insulator is through nano-sized superconducting dots patterned on top of the surface. This was evaluated according to a design described in the end of this chapter and required an extra step in the fabrication.

3.1 Hall bars

The normal resistance, carrier concentration and mobility were extracted from current-voltage relations using Hall effect measurements. For this, a current channel was designed from one end of the sample to the other, with two electrodes for measuring the longitudinal resistance situated on one side of the flake. On opposite sides of the flake, two additional electrodes were put to measure the Hall resistance. The design can be seen in Figure 3.1 where V_A, V_B, V_C and V_D indicate the electrodes where the voltage was measured and I the electrodes through which the current was sent. This layout is referred to as a Hall bar.

On each chip, five to nine Hall bars were designed. The flakes were fabricated through two different methods; exfoliation and direct patterning on top of the topological thin film. The fabrication techniques are described in Chapter 4.

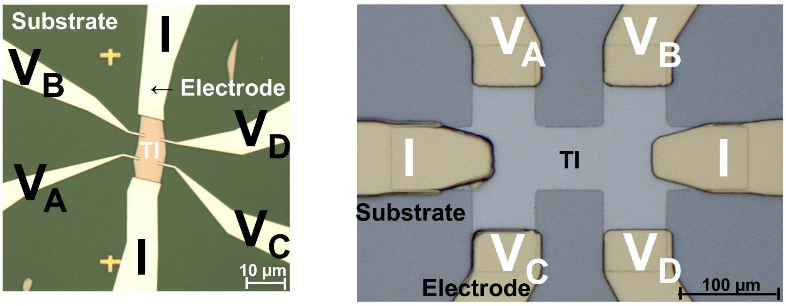

(a) Hall bar from exfoliation (b) Hall bar from direct fabrication

Figure 3.1: Microscope pictures of two Hall bars, used for current-voltage characteristics. The topological insulator on top of the substrate was contacted with six electrodes, two for current marked as I and four for voltage marked as V. The current was put through the current electrodes, marked with I. The voltage could be measured either along the current channel (V_{AB} or V_{CD}) or transverse (V_{AC} or V_{BD}). (a) The Hall bar is fabricated with exfoliation technique and (b) the Hall bar is fabricated through direct fabrication on the thin film.

When the flakes were fabricated through exfoliation, the chip layout had to be designed for each sample. The size of the exfoliated flakes limited the dimensions of the Hall bars to be 2-3 μm wide (between the Hall electrodes) and 4-6 μm long (between the current electrodes).

Using the direct fabrication, the same photo-mask was used for all samples. The width of the Hall bars were ranging from 2 μm to 20 μm. However, the 5 μm wide Hall bars were in general used for the growth characterization since the dimensions were comparable to the exfoliated flakes used for Hall measurements.

In both designs the electrodes reached from Hall bars to the contact pads, which were used to connect the samples to the measurement equipment with gold wire. The contact pads were designed to be large enough to contact the 25 μm gold wires with a micro-contact bonding machine.

The electrodes were usually made in gold and sometimes aluminum, while the topological insulator was etched or exfoliated from Bi_2Te_3 or the Bi_2Se_3. In general a silicon substrate was used, but sometimes also other semi-insulating materials. The thickness of the electrodes was 100-150 nm depending on the thickness of the topological insulator. The fabrication process is further discussed in the next chapter.

3.2 Josephson junctions

The Josephson junctions, seen in Figure 3.2, were used for low temperature measurements with topological insulators as the weak link. The electrodes were fabricated with superconducting aluminum. The dimensions were ranging between 1.5 μm and 4 μm for the width of the junction and between 150 nm and 350 nm for the distance between the superconducting electrodes. In the figure the Josephson junction was patterned directly on the Bi_2Te_3 thin film, with a 150 nm designed distance between the aluminum electrodes.

The topological insulator flakes had thicknesses between 50-80 nm. Therefore the alu-

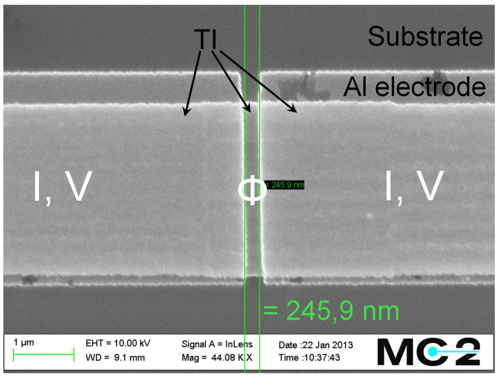

Figure 3.2: Josephson junction patterned directly on the Bi_2Te_3 thin film. The topological insulator flake was contacted with aluminum electrodes, where current was applied and voltage measured. A phase difference was created through the topological weak link between the superconducting electrodes.

minum electrodes were fabricated with a thickness of 90-100 nm to ensure good coverage over the edges. A limiting factor for the thickness of the electrodes was the resist used. The resist was chosen so that it was thicker than the desired aluminum for the lift-off to work and at the same time had good enough resolution. In addition, the aluminum had to cover the step of the flake for good contact and was also used to keep the flakes on the substrate.

3.3 Superconducting quantum interference devices

The SQUIDs were, as the Josephson junctions, fabricated with superconducting aluminum electrodes and topological insulators bridging them. Two main SQUID designs were considered with the same effective area. The two designs can be seen in Figure 3.3. The design in Figure 3.3(a) required that the whole loop was on top of a topological insulator film. The other SQUID design, shown in Figure 3.3(b), only required the junctions to be on top of the film. The latter geometry allowed flakes of smaller dimensions.

The SQUIDs were designed to have Josephson junctions with a distance around 300 nm between the superconductors. The area of the SQUID was designed to be 25 μm^2. The thickness of the flakes and the aluminum was the same as for the Josephson junctions in the previous section.

On the same samples, reference SQUIDs were also fabricated. The reference SQUIDs were designed with bridges of aluminum as weak links between the superconductors, instead of topological insulators. The widths of the bridges were between 200 nm and 300 nm, and the thickness was the same as the aluminum in the SQUIDs.

3.4 Nano-sized dots

Figure 3.4 shows the design for the nano-sized dots used to induce superconductivity into the topological insulator. They were fabricated in aluminum on top of the topological insulators in a geometry similar to the Hall bars in Figure 3.1.

The dimensions and geometry were chosen similar to Eley's work [33] with niobium nanodots on top of a gold thin film and from the experience gained during the thesis

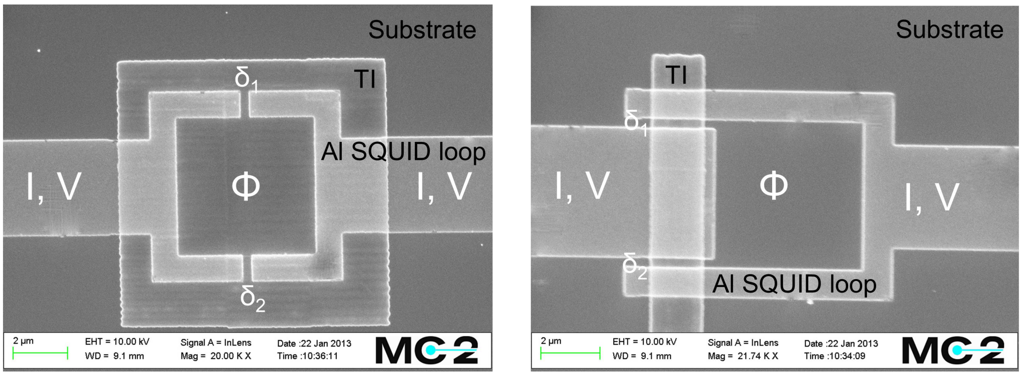

(a) SQUID design on top of film. (b) SQUID design party on top of film.

Figure 3.3: The two different designs of the SQUIDs, here fabricated with direct patterning on the thin film. (a) The SQUID was squared and the whole loop was on top of the flake. This required a larger flake. (b) The other design, where the flake was between the electrodes but the loop did not have to be on the flake.

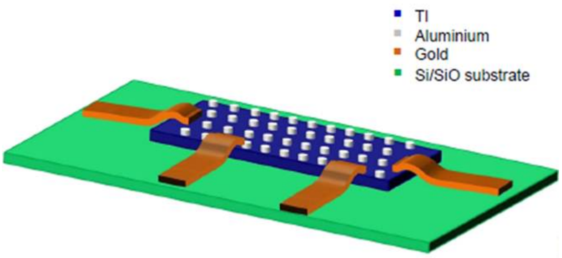

Figure 3.4: The aluminum dots were patterned on top of the topological insulator contacted with gold electrode as in the Hall bar design in Figure 3.1.

work on Josephson junctions. The hexagonally patterned dots had a thickness of 80 nm, a diameter of 100 nm and a distance between them ranging from 100 nm to 1.5 μm. As for the Hall bars, Josephson junctions and SQUIDs the thickness of the electrodes were limited by the thickness of the topological insulator thin film. Accordingly a thickness of 90 nm for the gold electrodes was designed.

4

Fabrication

THE FABRICATION PROCEDURES of the devices were developed during the thesis and were based on well established methods in the Quantum Device Physics group at MC2, Chalmers University of Technology. To fabricate the devices different techniques and procedures were used. An overview of this is presented in Figure 4.1 and the complete fabrication recipes can be found in Appendix A. Before the procedure is presented, the most important fabrication techniques used will be explained briefly.

4.1 Bi_2Te_3 growth

The aim of the Bi_2Te_3 growth was to optimize the parameters in order to achieve a topological insulating material with an insulating bulk and a conductive surface. Three different procedures were used to grow Bi_2Te_3 thin films with molecular beam epitaxy.

1. An amorphous mixture of bismuth and tellurium was deposited at a temperature of 120 °C. Then the temperature was increased to anneal to crystalline phase and the growth continued at temperature between 200-280 °C.

2. The substrate was first soaked for one minute in tellurium at a temperature below 200 °C. The growth continued directly on the soaked substrate at temperatures between 140-220 °C.

3. A monolayer of Bi_2Te_3 was grown directly on the substrate, of which the material and crystalline angle was varied. The substrate was then soaked in tellurium and another monolayer of Bi_2Te_3 was deposited. This process was repeated until the desired thickness was reached. This technique resulted in samples appearing milky, due to accumulation of tellurium on the surface. While the crystal thin film was grown, the tellurium accumulated on the surface because of a too high flux of tellurium.

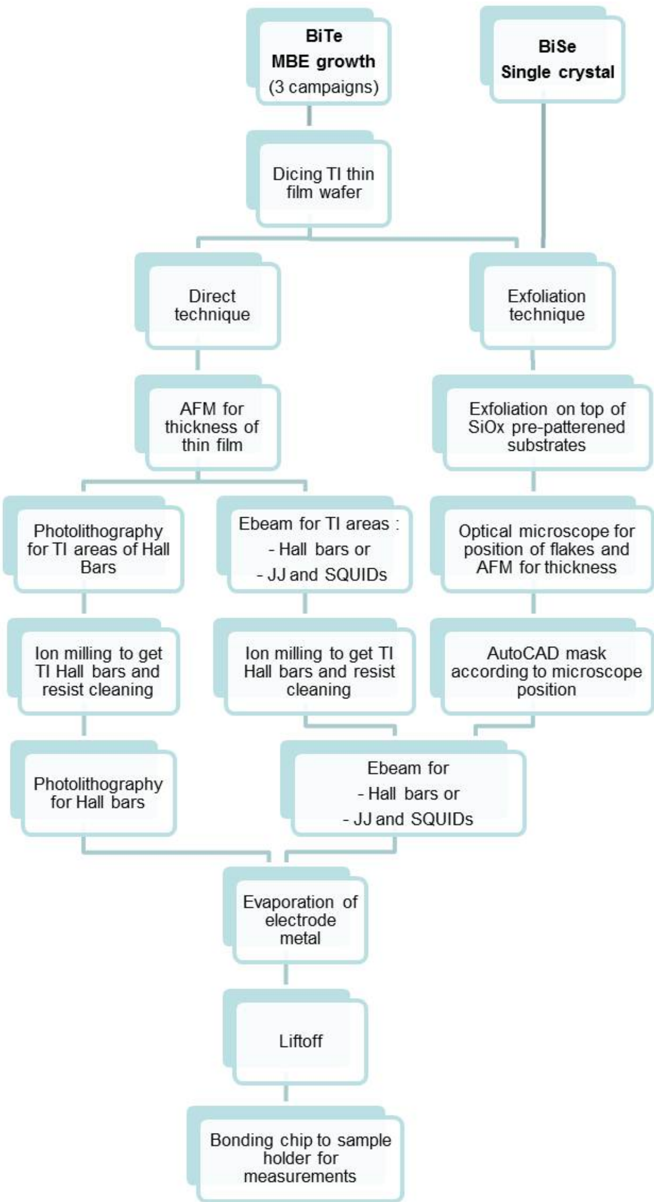

Figure 4.1: There were two main fabrication processes used after receiving the topological insulators; the one based on direct fabrication technique and the other one based on exfoliation technique. Direct fabrication could only be used on the Bi_2Te_3. In the exfoliation technique blue tape was used to transfer topological insulator flakes to the substrate and a new AutoCAD mask had to be drawn for every chip. In contrast, the direct fabrication was done with the same mask on each sample, but needed an addition step of ion milling to remove the unwanted topological insulator areas. The other steps in the techniques were similar with AFM, evaporation, liftoff and electron beam lithography. In addition, the direct fabrication enabled fabrication of Hall bars with photolithography, which was much faster than the electron beam lithography.

4.2 Fabrication techniques

Various fabrication steps and techniques were used. In this section the most important techniques used in the fabrication process will be explained.

4.2.1 Exfoliation

The exfoliation process was similar to the Scotch Tape technique commonly used for graphene and can be seen in Figure 4.2. The bonding mechanism between the quintuple layers in the topological insulator is weaker than within the quintuple, as described in Section 2.1.1. When the tape was applied to the crystal (Figure 4.2(a)) and then ripped off (Figure 4.2(b)), the favorable cleavage was between the quintuples. Some parts of the topological insulator got stuck on the tape. To make these pieces thinner the tape could be exfoliated from with another tape, but then the size of the flakes became smaller. The flakes were transferred, by pressing the tape on top of a pre-patterned substrate and removed, leaving flakes on the substrate (Figures 4.2(c),4.2(d)).

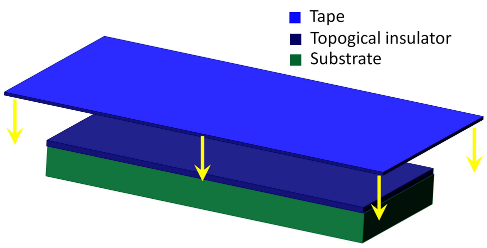

(a) The tape was put on the TI.

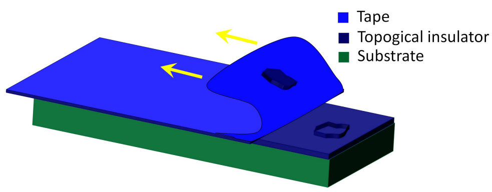

(b) The tape was ripped off.

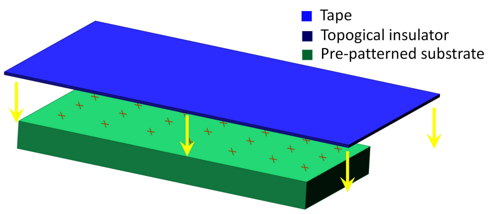

(c) The tape was put on a pre-patterned substrate.

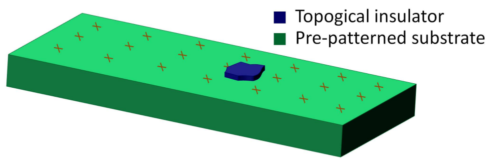

(d) The TI flake was left on the pre-patterned substrate.

Figure 4.2: The topological insulator flake was obtained by exfoliation from either a single crystal or a thin film, as shown here. (a) The tape was put on top of the topological insulator and a cotton swab was used to increase the proximity. (b) The tape was ripped off the topological insulator, removing flakes from it. (c) The tape with flakes was pushed against a pre-patterned substrate. (d) When the tape was removed, some flakes were left on the pre-patterned substrate.

The flakes were of different shape and differently distributed every time. For this reason the pattern on each sample was different. Optical microscopy was used to localize the flakes and atomic force microscopy was used to determine the thickness of the flakes, which limited how thin the electrodes could be.

4.2.2 Direct patterning

In figure 4.3 the direct pattering technique is illustrated. This technique could only be used on the Bi_2Te_3 thin films grown by MBE on insulating substrates. The direct fabrication was done by covering the sample with resist (Figures 4.3(a),4.3(b)) and patterning with either photolithography or electron beam lithography (Figure 4.3(c)). After patterning, the resist was developed (Figure 4.3(d)) and the unwanted topological insulator areas were removed with ion milling (Figure 4.3(e)). In a last step, the sample was clean (Figure 4.3(e)) leaving only the desired topological insulator pattern.

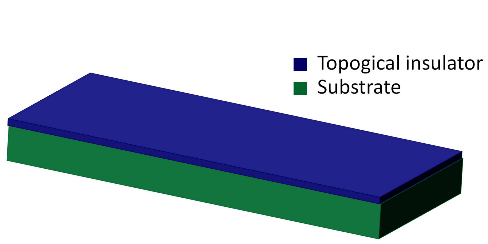

(a) Topological insulator thin film.

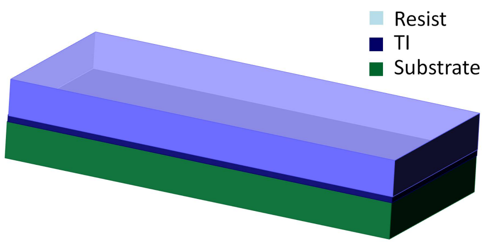

(b) Resist was spun on top.

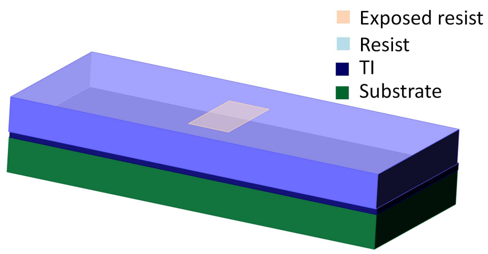

(c) The resist was exposed.

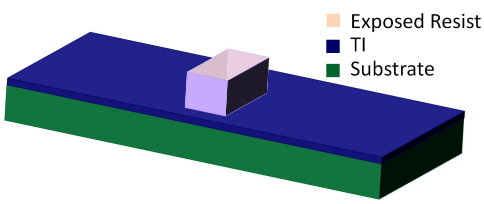

(d) Development removed unexposed resist.

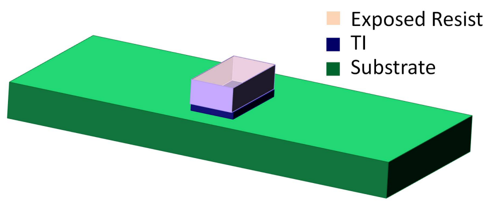

(e) The uncovered TI was milled away.

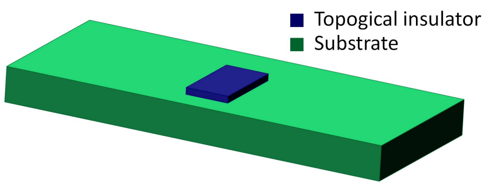

(f) Cleaning of the resist left the desired TI area.

Figure 4.3: The thin films of Bi_2Te_3 could be patterned directly. (b) The thin film was covered with negative resist. (c) The desired area was exposed by either electron beam- or photolithography. (d) Development removed the unexposed resist and these parts of the topological insulator uncovered. (e) The sample was ion milled, which removed the uncovered topological insulator. (f) After cleaning the resist, the sample had the desired topological insulator pattern on top of the substrate where the thin film was grown.

4.2.3 Ion milling

To remove the topological insulator thin film from where it was not patterned, argon ion milling was used. In ion milling, the sample was bombarded with ions. This technique was used because argon is the most inert gas and does not leave argon residues on the sample. The resist, covering the patterned topological insulator, was milled away much slower than the topological insulator. In this way the topological insulator was left only where is was patterned.

4.2.4 Photolithography

When the structures to be patterned were larger than a few microns, photolithography could be used. Photolithography was then used in two steps; for direct patterning on top of the topological thin films as in Figure 4.3 and after this for patterning of the electrodes on top of the topological insulator pattern as in Figure 4.4.

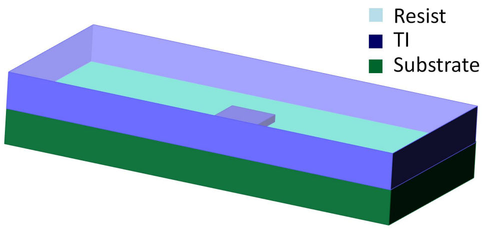

(a) The TI was covered with resist.

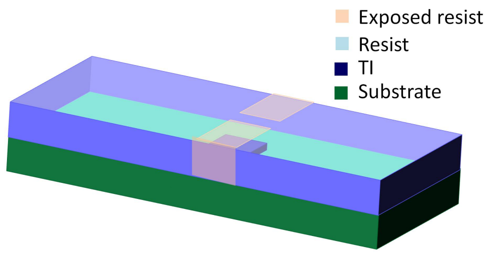

(b) The resist was exposed.

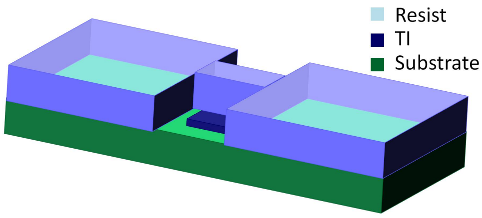

(c) Developement removed exposed resist.

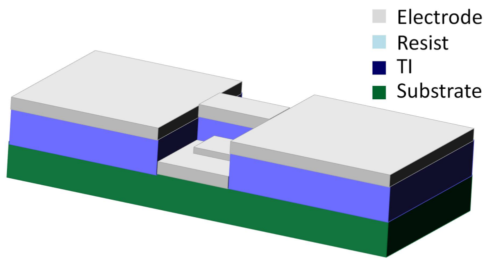

(d) The electrode metal was evaporated.

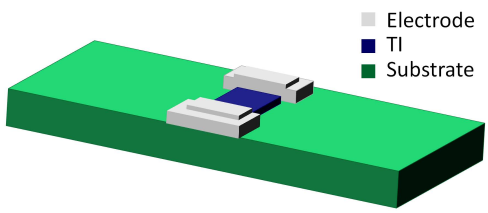

(e) The metal on top of the resist was removed through a liftoff process, leaving the desired device on the substrate.

Figure 4.4: The topological insulator flake, recieved either by direct patterning or exfoliation, was contacted through a lithography process. (a) The sample was covered with positive resist. (b) The desired area was exposed by either electron beam- or photolithography. (c) Development removed the exposed resist. (d) The metal for the electrodes was evaporated and covered the whole sample. (e) The metal on top of the resist was removed through liftoff and the desired device was obtained.

The photolithography process limited the design in two main ways; the pattern size and the disability to vary the design of the pattern. Therefore photolithography could only be used when fabricating Hall bars directly on top of the Bi_2Te_3 thin film. Since the Hall bars were fabricated directly on top of the thin films, the substrate on which the thin films were grown had to be semi-conducting in order to enable measurements of only the thin film topological insulator. The substrate material was usually silicon but also gallium-arsenide.

In photolithography a pre-designed mask was positioned over a sample covered in photo-resist. The UV photosensitive resist was also very sensitive to moister. Therefore the chips were pre-baked to dry the surface, before the photo-resist was spun on the sample as in Figure 4.4(a). The sample was baked to harden the resist and remove moisture from it.

Some regions of the mask were transparent to the ultraviolet light. These areas allowed the underlaying parts of the sample to be exposed (Figure 4.4(b)), while the non-transparent areas of the mask blocked the UV light. Exposure to UV light broke the polymer chains in the photo-resist and made it more soluble. A developer could then be used to remove the exposed resist, leaving the unexposed resist on the sample as in Figure 4.4(c).

When the resist was spun it was very thick and uneven at areas near the edges of the sample. Therefore the outer part of the chip was first exposed and developed to remove the resist edge. The next photolithography step could then be performed with better precision. Depending on the fabrication step, either the topological areas or the electrodes were patterned.

Since the topological areas were patterned first, this photolithography-mask also included alignment marks for aligning electrodes fabricated with a following photolithography step.

Alignment and reference marks

The alignment marks were used to align the following pattern with the previously exposed one. This alignment was very important in order to ensure contact between the electrodes and the topological insulators. Therefore alignment marks were also used in electron beam lithography in order to orientate the position of the electron beam on the sample.

An additional sets of marks were designed for the exfoliation fabrication process. These marks were referred to as reference marks and were designed on the silicon substrates on which the topological insulator flakes were transferred to. The reference marks were used to localize the flakes with an optical microscope. Using the information about the flakes position, an AutoCAD drawing for the electrodes could be designed accordingly.

4.2.5 Electron beam lithography

In electron beam lithography, electrons were used for exposure instead of the photons in photolithography. Since electron beam lithography is not limited by the diffraction of light, smaller structures such as Josephson junctions, SQUIDs and nanodots could be patterned. The pattern resolution could be to a tens of nanometers depending on the underlying substrate. Electron beam lithography was used for direct patterning of topological insulators as in Figure 4.3, but mainly on exfoliated flakes (Figure 4.2) for patterning of electrodes according to Figure 4.4.

Similarly to photolithography the samples were spun (Figure 4.4(a)) and baked with two polymer based resists, which are sensitive to electrons. Since the electron beam exposed the samples according to an AutoCAD drawing (Figure 4.4(b)), the desired pattern could be varied. The flexibility in design was important in the exfoliation fabrication, where the flakes were randomly distributed and a new mask had to be drawn for each sample.

There were two types of resists that could be used; a positive and a negative. The positive resist is described in the previous section. When a negative resist was used, the exposure caused cross-linking between the polymers and these areas were less soluble. After development (Figure 4.4(c)) the opposite pattern to the drawing was left on the sample.

4.2.6 Development and undercut

When the samples were developed after exposure with photolithography or electron beam lithography, a solvent was used to remove the exposed (positive) or unexposed (negative) resist from the sample. In electron beam lithography for electrodes, two resists were used and two solvents for development were used. First, the top resist was developed, leaving the top resist on areas according to design. This opened up holes in the top resist, where the underlaying resist could be developed in a second solvent.

The underlaying resist was developed with a different solvent to create an undercut. An undercut is the hole created from the uniformed removed underlaying resist, under the top resist. Since the hole in the top resist was smaller than the hole in the underlaying resist, the evaporated metals on the sample could not stick to the walls of the underlaying resist. In this way the evaporated metals for the electrodes was not removed with the resist in the lift-off process.

4.2.7 Ashing

The samples were ashed with oxygen plasma to remove organic materials and residues of unexposed resist. The benefit of oxygen plasma is its high reactivity with organic materials, while it less reactive with un-organic materials. In this way the samples could be cleaned without destroying the patterned devices. After ashing, the samples were ion milled during a short (10 sec) time to further clean the surface by removing the top layers.

4.2.8 Evaporation

All metal structures in the designs were deposited by thermal evaporation (Figure 4.4(d)), a commonly used technique for low temperature superconductors. Evaporation was preferred instead of sputtering, because of the directionality of the process. This is optimal for a lift-off process.

In thermal evaporation, a source with the desired metal was heated with either a laser gun, a electron gun or a electric current. When the source was hot enough, the material evaporated. The evaporating metal gas spread uniformly in the vacuum pumped chamber and covered the whole sample. The thickness was monitored by a quartz crystal sensor positioned nearby the sample. When the mass of the sensor changed due to the evaporated metal on it, the frequency of the sensor changed and this was converted to a film thickness.

4.2.9 Lift-off and cleaning

To remove the unwanted metal, which was on top of the resist, the sample was put in a solvent. When the resists was solved only the metal on top of it was removed. The metal that had been evaporated on top of areas without resist, was left on the sample after the development. This is called a lift-off process and can be seen in Figure 4.4(e). If only resist had to be removed and no metals had been evaporated on top of the resist, this process is called cleaning and can be seen in Figure 4.3(f). For instance cleaning of the sample was used after ion milling the directly patterned topological insulator areas.

4.3 Fabrication procedures

The samples were fabricated according to Figure 4.1 in the MC2 cleanroom, in mainly the following procedures. The recipes can be found in Appendix A.

Two topological insulators were used; Bi_2Se_3 single crystal from Japan and Bi_2Te_3 thin films from Chalmers University of Technology. The topological insulators were either obtained through direct patterning on top of the thin films or through exfoliation and transfer to a pre-patterned substrate.

- On the MBE grown Bi_2Te_3 thin films both exfoliation and direct patterning could be used. The direct patterning, illustrated in Figure 4.3, was done with either photolithography or electron beam lithography. After patterning the samples were ion milled, which removed the topological insulator from areas that was not in the pattern.
- The exfoliation process could be used on both the single crystal Bi_2Se_3 and the thin film Bi_2Te_3. Before the exfoliation and transfer, the silicon substrates had to be prepared. In either photolithography or electron beam lithography, alignment and reference marks were patterned on the substrates. To save time many identical substrates were made at the same time on a wafer. A thin layer of chromium and a layer of gold were deposited on the whole silicon/silicon oxide wafer by evaporation. The thin layer of chromium was used underneath the gold to make it stick better to the substrate. The alignment and reference marks were made in the gold (and chromium underneath), since gold is a stable metal that gives a detectable signal in scanning electron microscopy.

  After lift-off and dividing the wafer into chip-sized substrate, the exfoliation from the topological insulator and transfer to the substrates could be done. This is illustrated in Figure 4.2. Since the flakes were randomly distributed they had to be localized with the optical microscope before designing the AutoCAD drawing. Depending on which type of information was desired the different circuit elements described in Chapter 3 were included in the design.

When the topological insulator patterns were obtained by either of the two methods, the samples were cleaned. The fabrication continued with patterning of the electrodes according to the steps in figure 4.4. In general, the samples fabricated for Hall measurements in order to characterize the growth were fabricated with photolithography, while the Josephson junctions and the SQUIDs were fabricated with electron beam lithography.

The exposed resist, by either lithography method, was removed with development. The samples were ashed with oxygen plasma to remove organic molecules and resist residues. Before evaporation of metal for the electrodes, the samples were ion milled to remove the top layer of the surface for better adhesion with the metal layer. The unwanted evaporated metals on top of the resist was removed with lift-off, leaving the sample with the fabricated device. The device was finally inspected with an optical microscope to ensure successful fabrication.

4.4 Nano-sized dots

The topological insulator and electrodes for the nanodot design described in Chapter 3.4 were fabricated with photolithography in the same procedure as the Hall bars. In an additional electron beam lithography fabrication step, the nano-sized dots were designed.

This additional fabrication step was done in the same was as the electrodes for Josephson junctions and SQUIDs, meaning that the process in Figure 4.4 was used one more time. The resist was spun, exposed by electron beam lithography and developed. Afterwards the aluminum was evaporated and a lift-off process left the desired hexagonal nano-sized dot pattern on top of the topological insulator.

5

Measurements

THE TOPOLOGICAL INSULATORS were characterized by transport measurements, spectroscopy and topography measurements. The transport measurements were done on samples with the design and from the fabrication process described in Chapters 3 and 4. In these designs superconducting structures were used to measure the topological insulator and therefore cryogenics were needed.

The spectroscopy and topography measurements were conducted after cleaving directly from the thin films or crystals. Without any further fabrication the topological insulators were measured using a scanning tunneling microscope with Maria Iavarone's group at Temple University in Philadelphia, US.

5.1 Cryogenics

To measure the superconducting structures the samples need to be cooled down to temperatures lower than the evaporated materials' critical temperature. A film of aluminum has a critical temperature of 1.18 K [34], requiring cryogenics for measurements in the superconducting regime of the electrodes.

Two different cryogenic systems were used to cool down to low temperature. In the Quantum Design physical property measurement system (PPMS) liquid nitrogen was used to keep the inner dewar with liquid helium cold and in this way reduce the helium consumption. The liquid helium was used to enable measurements down to 2 K. A superconducting magnet was used, enabling measurements in high magnetic fields up to 14 T. The magnet was made by NbTi cable with copper coating. During operation it was kept cold by immersion in liquid helium.

To reach lower temperatures another technique was used in Oxford Instruments' HelioxVL Cryostat. The technology is based on a gas liquid system. The gas molecules have higher energy than the molecules in the liquid. If the gas molecules are removed the average energy per molecule in the system is decreased. Due to the vapor pressure, molecules from the liquid have to phase-shift to gas. The transition requires energy, which is absorbed from the system and cools it. This type of cooling, electron cooling, using helium-4 makes it possible to reach 1 K.

The helium-3 has a lower boiling temperature, and a lower mass. Hence helium-3 has phase transitions at different pressures and energies. Helium-3 electron cooling can reach

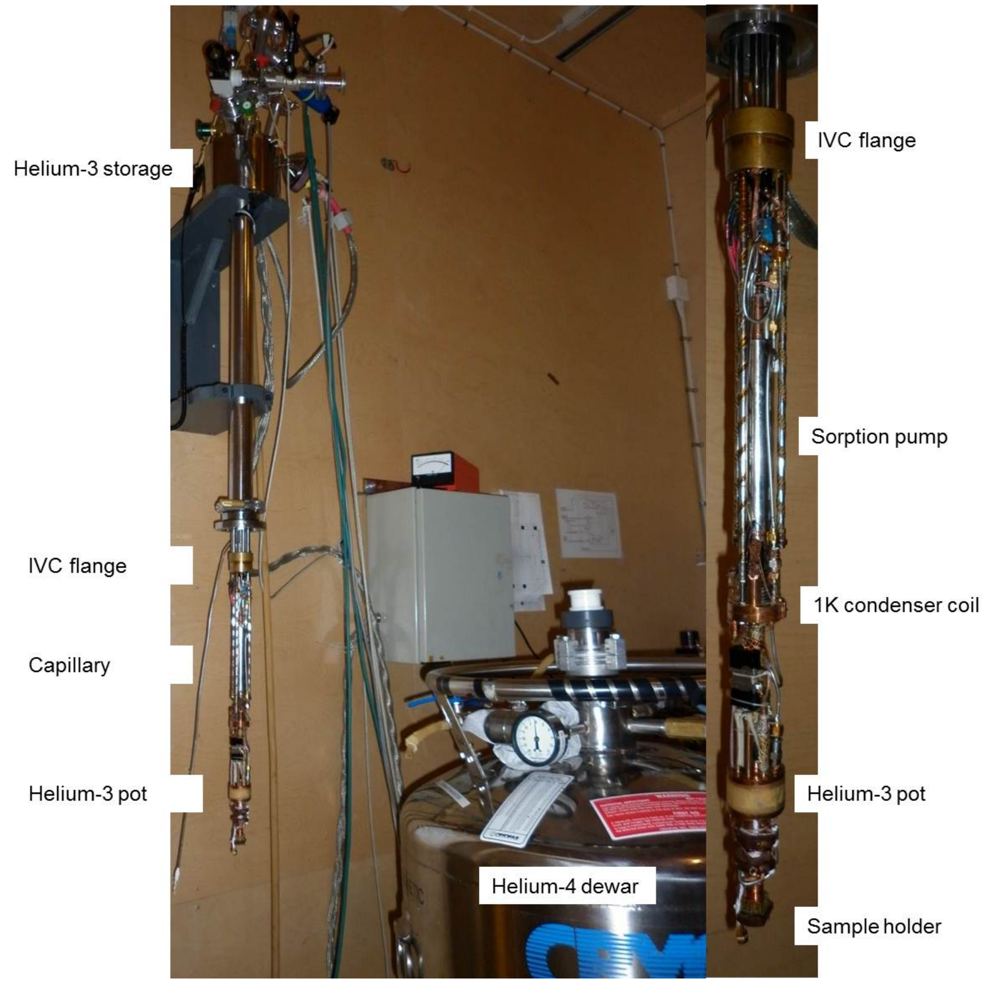

Figure 5.1: The dipstick that was put in the helium-4 dewar. The different parts of the cryostat are named on the dipstick and on a zoomed in picture of the inner part.

250 mK. At this temperature the aluminum, used for electrodes, was superconducting.

The cooling in the cryostat was done in steps and the dipstick, that was put in the helium-4 dewar, can be seen in Figure 5.1. The sample was put in the coolest part of the cryostat, enclosed by the inner vacuum chamber, IVC. The IVC was attached on the IVC conical shaped flange, which was greased to decrease leakage. Sealed, the IVC was pumped and vacuum was kept in the IVC.

The first main step of cooling down was to reach 4.2 K, using a helium dewar. The IVC was put in the 4.2 K liquid helium bath, which worked as a heat sink. A little volume of Helium-4 exchange gas was let inside the IVC to conduct heat away from it to the bath.

In the second step the helium-4 gas was pumped out through a capillary to the 1 K pot by opening the needle valve. Pumping to the 1 K pot, the liquid helium-4 started to evaporate to re-establish equilibrium. The phase shift from liquid to gas extracted heat and since the 1 K pot was thermally decoupled from the helium-4 bath it could reach approximately 1.6 K.

Helium-3 is in a closed circuit in the cryostat. When the temperature of the 1 K pot reached the lowest temperature, the helium-3 condensed on it, through the 1 K condenser

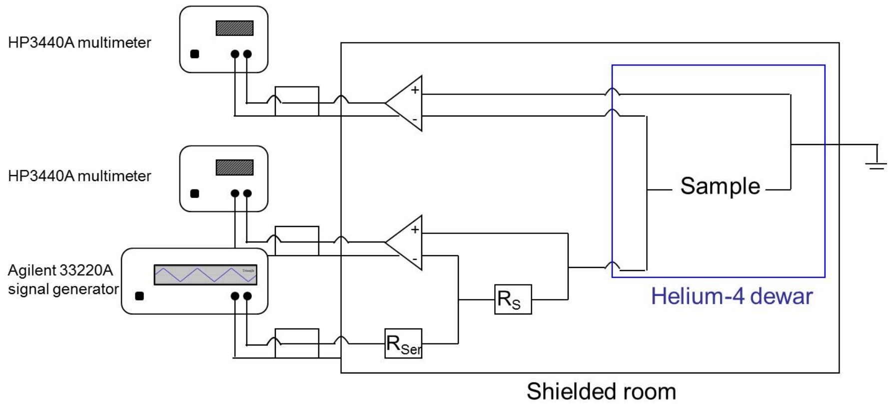

Figure 5.2: The sample, put in the Helium-4 dewar, was contacted through the magnetic shielded room to the amplifiers. The current bias was created as a voltage signal over the resistance R_{Ser}. The output voltage was measured directly, while the current was measured as a voltage over the resistance R_S. Both the output signals were amplified before measured with the multimeters.

coil and was collected in the helium-3 pot inside the IVC.

The last step of cooling down to 300 mK was done by evaporative cooling on helium-3 using the sorption pump. It is a molecular pump made out of charcoal in a small cylinder. When the temperature was below 30 K the charcoal absorbed helium-3 gas molecules from the helium-3 pot. The vapor pressure on the liquid helium-3 was then lowered. This results in a phase shift of the helium-3 liquid molecules which requires heat and lowers the total temperature of the helium-3 pot. When the charcoal was heated the absorption of helium decreased and the cooling of the system stopped.

The sample could be kept cold as long as there was still liquid helium in helium-3 pot. After that the 1 K pot needed to be condensed.

5.1.1 Measurement set-up

A crucial point of all measurements is noise reductions. The helium-4 dewar therefore contained a μ-metal. This is a nickel-iron alloy with high magnetic permeability and can hence protect against static and low-frequency magnetic fields. In addition the helium-4 dewar also contained a superconducting magnetic shield. The entire cryostat was placed in an electromagnetic shielded room while the multimeters were placed outside as seen in Figure 5.2.

Four point measurements were conducted; two contacts were used to apply current and two for voltage measurement. This technique enabled measurements of only the resistance of the device.

The electronic set-up can be seen in Figure 5.2. The sample was measured using current bias. A sawtooth voltage was generated by a signal generator Agilent 33220A and applied over a bias resistance, R_{Ser}. This created a limited current that was fed into the device. The R_{Ser} was chosen between 100 kΩ and 1 MΩ to be much larger than the total impedance of the rest of the system.

The voltage over the device was measured directly, while the current was measured as the voltage over a resistance, R_S. The value of R_S was chosen in parallel to the value of the amplification. Both output signals were amplified with the Princeton Applied

Research 5113 Battery driven differential pre-amplifiers before they were measured with two HP3440A Multimeters.

In addition to the measurement set-up in Figure 5.2 a copper coated niobium coil was put under the sample holder inside the helium-4 dewar. Niobium has a critical temperature of 10 K [34] and was superconducting in the liquid helium-4 bath. The build in modification enabled magnetic field measurements. A Yokogava 7651 programmable DC-source drove a current through the copper coated niobium wire in the helium-4 dewar. This generated a magnetic field with 86 mT/A, resulting in a magnetic field strength up to ± 10 mT.

The electromagnetic field measurements were done as the magnetic field measurements, but with an AC source instead of a DC source. The AC source signal had a radio-frequency in the range of 0.1 GHz to 20 GHz with varying amplitude from -135 dbm to 16 dbm.

In conclusion, the measurements were performed in cryostat enabling sub-Kelvin temperatures. This required both helium-3 and -4, together with evaporative pumping techniques. The noise was reduced by a magnetic shielded room and a magnetically shielded helium-4 dewar. The current fed into the devices was limited by a resistor and the measured current was measured as a voltage over a resistor. The voltage was measured directly. The current-voltage characteristics were investigated in the presence of an applied magnetic field and as a response to microwave radiation. The temperature dependence of the current-voltage characteristic of the devices was also examined.

5.2 Scanning tunneling microscope

The scanning tunneling microscope measured the tunneling current between a conductive tip and a conductive sample, while raster scanning under constant applied voltage. In Figure 5.3 the scanning tunneling microscope used can be seen. It was enabled operations at cryogenic temperatures and in ultrahigh vacuum.

To enable measurements with this sensitive microscope, the surface of the sample had to be clean. Therefore the surface was cleaved in a 10^{-8} Torr vacuum pumped pre-chamber with an excessed flow of nitrogen. This was done by silver epitaxy gluing a screw on top of a 1x1 mm sample. The screw was then perpendicularly pushed off the sample. If the adhesion was larger than between the Bi_2Te_3 layers, a clean surface was produced and could be used for measurements.

After a clean and relatively flat surface was achieved, the sample was moved with the manipulators through the manipulation chambers to the sample holder in the scanning tunneling microscope chamber. The sample could then be cooled down by the build-in cryostat down to 300 mK.

To minimize mechanical vibrations the system was located on a vibration damped table. The scanning tunneling microscope was enclosed in a shielded room to protect from electromagnetic and magnetic fields from the surroundings.

Based on ultrahigh vacuum techniques the system had the ability to reach pressures below 10^{-9} Torr. This is needed since the measurements were very sensitive to absorption of molecules on the surface of the samples and molecules disturbing conduction of the tip.

Despite the cleaving process the Bi_2Te_3 had a relatively large roughness and hence the constant current mode was used. The sample was then scanned using a feedback

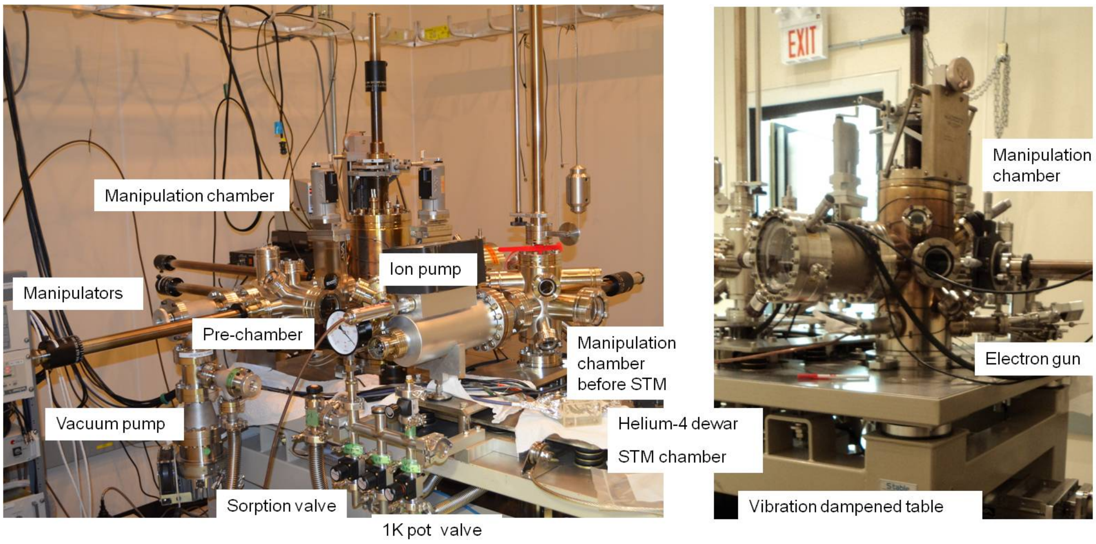

Figure 5.3: The scanning tunneling microscope used, with a build in cryostat enabling measurements down to 300 mK. In addition this STM operated at ultrahigh vacuum and the sample could be manipulated before in two vacuum pumper chambers. One with ability to evaporate materials and conduct LEED measurements.

loop to keep the current constant. This forced the tip to move up and down, which gave the topography image of the charge density at the surface.

Spectroscopy was achieved by removing the feedback and moving the tip up and down on one position on the sample. This mapped the electron wavefunction outside the surface and was used to find the Dirac cone of the topological insulators.

6

Results and discussion

After design, fabrication and optical microscope inspection the devices were tested at room temperature to ensure working electrical contacts. With Hall measurements at temperatures down to 2 or 5 K, the Bi_2Te_3 growth was characterized. During the optimization of the growth the volume carrier concentration improved from 1 x $10^{21}\,\mathrm{cm}^{-3}$ to 4.4 x $10^{18}\,\mathrm{cm}^{-3}$ and the mobility from $150\,\mathrm{cm^2/Vs}$ to $5500\,\mathrm{cm^2/Vs}$, which is close to the values for Bi_2Se_3 single crystal.

The samples with the lowest carrier concentration and highest mobility were used in devices for proximity measurements. Proximity measurements were performed on Bi_2Te_3 and Bi_2Se_3 devices at sub-kelvin temperatures. Current-voltage (IV) characteristics were measured as a function of electromagnetic response, magnetic field and temperature.

One Bi_2Te_3 thin film was also charactrized with topography and spectroscopy measurements by scanning tunneling microscope. This revealed a roughness of 0.6 nm on the cleaving area and indicated a Dirac cone at 300 meV.

6.1 Bi_2Te_3 growth characterization

The carrier concentration and the mobility of the Bi_2Te_3 thin films have been obtained by measurements of the Hall resistance and longitudinal resistance according to Figure 3.1 in Chapter 3.1 in PPMS, described in Chapter 5.1. In Figure 6.1 the Hall resistance as a function of the magnetic field is shown for various Bi_2Te_3 samples.

The two contacts used for the Hall measurements were never exactly in front of each other, resulting in an additional small longitudinal resistance to the measured Hall resistance. By using measurements in both negative and positive magnetic field the longitudinal contribution could be removed. In this way the Hall resistance was extracted.

The sign of the Hall coefficient R_H, described in equation 2.1 in Chapter 2.2, determines the type of charge carriers. As seen in Figure 6.1, the data are following a line with negative slope, implying that negative charge carriers are dominating the transport in the topological insulators. Bi_2Te_3 is predicted to be p-type, i.e. to have positive charge carriers, with a volume carrier concentration around $10^{19}\,\mathrm{cm}^{-3}$ [35]. The measurements performed on samples from all three growth processes show n-type Bi_2Te_3, which suggests an excess of tellurium [35]. The tunability of the transport type was measured with

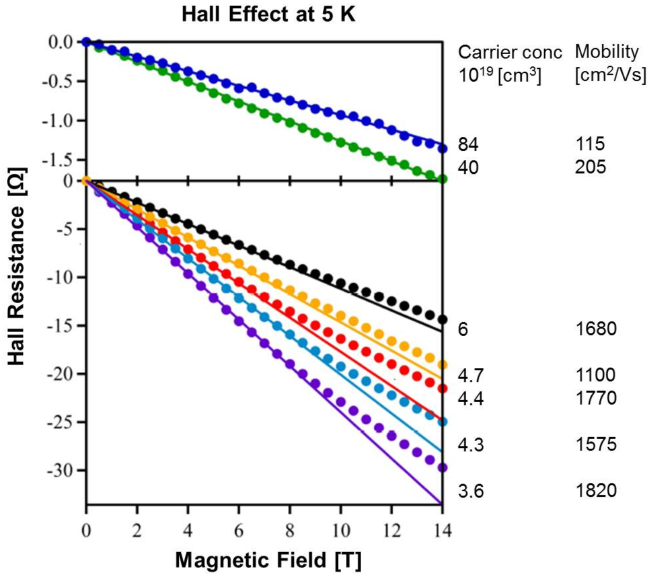

Figure 6.1: The Hall resistance measured in a perpendicularly applied magnetic field at 5 K. The dark blue curve was from a sample from the first growth process and was the most characterized sample, hence used as a reference. The other samples were grown with the second growth process, with variable growth conditions but all on Si(111). The markers are data points from measurements made in magnetic field up to 14 T, while the lines are linear extrapolations from low field (below 5 T) measurements.

ARPES measurements and shows that it is correlated with a change from layer-by-layer growth to step-flow [36].

The carrier concentration was calculated from the Hall coefficient, according to equation 2.1 in Chapter 2.2. When one type of charge carriers are present the Hall coefficient is well defined and independent on the magnetic field. The Hall resistance is in this case linear. In Figure 6.1 the lines are linear extrapolations of measurements done up to 5 T. The linear fits did not coincide perfectly with the data points from measurements done up to 14 T, implying more than one type of charge carrier. This difference was more prominent for the purple and light blue curves in Figure 6.1, which are from samples with lower carrier concentration and higher mobility. Since the signatures of the surface requires a low carrier concentration and high mobility to be observed in addition to the bulk, the two types of charge carriers can be assumed to be from both the surface and from the bulk. For samples with higher carrier concentration, the surface transport was screened by the bulk.

The bulk conduction arises from vacancies and crystal defects. The three growth processes focused on obtaining the best quality crystal using different growth temperature, flux ratio and growth technique as mentioned in Chapter 4.1. A similar growth process used by Yu *et al* [37], after which they could demonstrate surface conduction. More importantly a separation between the top and bottom surface was measured though gate dependent Shubnikow-de Haas oscillations. During the thesis gating with electrolyte was tested in addition to Hall measurements on Bi_2Te_3 thin films from the first growth process. However, the surface was still by the bulk and the electrolyte used between the gate and the sample reacted with the surface. The gating with electrolyte and co-planar gates tested is described in Appendix C.1.

When calculating the carrier concentration, the thickness of the topological insulator was used. Atomic force microscopy was used to determine the thickness of exfoliated flakes. A roughness of 10 nm was revealed for 80-150 nm thick films, resulting in an uncertainty of 13 % of the thickness of the flakes. The Bi_2Te_3 thin films were grown on relatively rough substrates. This affected the growth, hence the smoothness of the thin films. The uncertainty in thickness transfer to an uncertainty when determining the carrier concentration.

The longitudinal resistance was measured using two contacts along the injection current, i.e. on the same side of the Hall bar seen in Figure 3.1 in Chapter 3.1. The conductivity was calculated from knowledge about the dimensions of the sample and according to $\sigma = \frac{\text{length}}{\text{cross section} \times \text{londitudinal resistance}}$. The mobility of the samples was calculated from equation 2.2 in Chapter 2.2.

The summary of the results is shown in table 6.1. The mobility and carrier concentration were compared from different growth methods. Depending on the results, the following growth process was planned with the growers. The best sample had a volume carrier concentration of 4.4 x 10^{18} cm^3 and a mobility of 5500 $^{\text{cm}^2}/_{\text{Vs}}$, which is comparable to the values from Bi_2Se_3 flakes exfoliated from single crystal. Oscillations described by the Shubnikov-de Haas effect, described in Chapter 2.2.2, were observed on Bi_2Se_3 when performing Hall measurements in magnetic fields up to 14 T. However, the same type of measurements performed on devices with Bi_2Te_3 did not show oscillations.

Table 6.1: The summarized results from devices fabricated with topological insulators from the Bi_2Te_3 growth processes and the Bi_2Se_3 single crystal. The results are extracted from Hall measurements.

	Flake thickness	Carrier Concentration	Mobility
Bi_2Te_3 first growth	70-160 nm	4-100 x 10^{19} cm^{-3}	50-2700 $^{\text{cm}^2}/_{\text{Vs}}$
Bi_2Te_3 second growth	25-70 nm	3-600 x 10^{19} cm^{-3}	35-3050 $^{\text{cm}^2}/_{\text{Vs}}$
Bi_2Te_3 third growth	40-100 nm	0.4-100 x 10^{19} cm^{-3}	220-5500 $^{\text{cm}^2}/_{\text{Vs}}$
Bi_2Se_3 single crystal	20-125 nm	1-10 x 10^{19} cm^{-3}	2000-5000 $^{\text{cm}^2}/_{\text{Vs}}$

The carrier concentration and mobility were used to characterize and optimize the molecular beam epitaxy growth of Bi_2Te_3. The parameters used to optimize the growth were the growth temperature and the growth Te/Bi flux ratio. The result of the second growth process can be seen in Figure 6.2, where the Bi_2Te_3 is grown on top of silicon (111) semi-insulating substrates.

The optimal growth temperature was 180 °C for a Te/Bi flux ratio of 17 according to Figure 6.2(a) and the optimal Te/Bi flux ratio was around 130 for a temperature of 180 °C according to Figure 6.2(b). During the optimization of the growth the volume carrier concentration improved from 1 x 10^{21} cm^{-3} to 4.4 x 10^{18} cm^{-3} and the mobility from 150 $^{\text{cm}^2}/_{\text{Vs}}$ to 5500 $^{\text{cm}^2}/_{\text{Vs}}$.

6.1.1 Hall measurements of devices fabricated with the exfoliation technique or the direct patterning.

Bi_2Te_3 Hall bars were fabricated with both the exfoliation and direct fabrication through photolithography. A comparison between the two fabrication methods is presented for

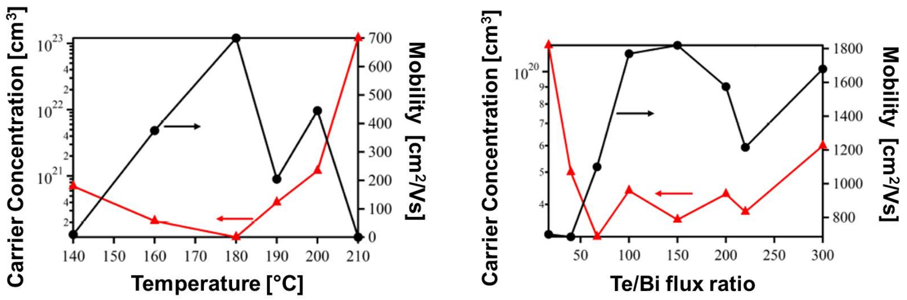

(a) Optimizing temperature (b) Optimizing Te/Bi flux ratio

Figure 6.2: The growth temperature and the Te/Bi flux ratio was optimized in the second growth campaign with samples grown on Si (111). In Figure 6.2(a) the temperature dependence showed minimal carrier concentration and maximum mobility for a temperature of 180 °C when the Te/Bi flux ratio was kept at 17. In Figure 6.2(b) the flux ratio was varied for a growth temperature of 180 °C. The optimal carrier concentration and mobility was obtained for a flux ratio around 130 .

the longitudinal resistivity in Figure 6.3 and for the Hall measurements in table 6.2. The longitudinal resistance of the devices was measured with temperature, resulting in similar values at temperatures below 60 K, but lower in the directly patterned devices at higher temperatures. The Hall measurements resulted in carrier concentrations and mobility of the same order of magnitude.

Table 6.2: Carrier concentration and mobility of devices fabricated from the same Bi_2Te_3 thin film, one with the exfoliation technique and two with the photolithography direct patterning.

Fab. techn.	Carrier Conc.	Mobility
Exfoliated	4.4 x 10^{18} cm^{-3}	5500 cm^2/Vs
Direct	8.3 x 10^{18} cm^{-3}	5200 cm^2/Vs
Direct	6.9 x 10^{18} cm^{-3}	6200 cm^2/Vs

The Hall resistance was evaluated at a temperature of 5 K and a magnetic field up to 5 T. The carrier concentration was calculated from the Hall resistance (eg Hall coefficient) and thickness of the topological insulator according to equation 2.1. A value of 4.4 x 10^{18} cm^{-3} was estimated for the device fabricated with exfoliation. The directly patterned devices the Hall bars were measured twice in two different cool downs in the PPMS measurement system. The carrier concentrations, 8.3 x 10^{18} cm^{-3} and 6.9 x 10^{18} cm^{-3}, from these Hall bars were slightly larger than from the exfoliated one. The value of the carrier concentration was inversely proportional to the thickness, hence the uncertainty in thickness mostly due to the roughness of the films influenced this value. The directly patterned devices usually had thicker topological insulators, since the exfoliation takes place between the quintuples leaving parts of the film on the growth substrate. In table 6.2 this deviation is accounted for.

The mobilities from the two measurements on directly patterned Hall bars differed the same amount from each other as from the exfoliated device. A mobility of 5500 cm^2/Vs was estimated for the exfoliated topological insulator, while the same values for the directly patterned devices were 5200 cm^2/Vs and 6200 cm^2/Vs. The mobility was calculated from equation 2.2 and did accordingly depend upon the thickness, length and width of the Hall bars.

Also, when the longitudinal resistivity (Figure 6.3) was evaluated, the thickness,

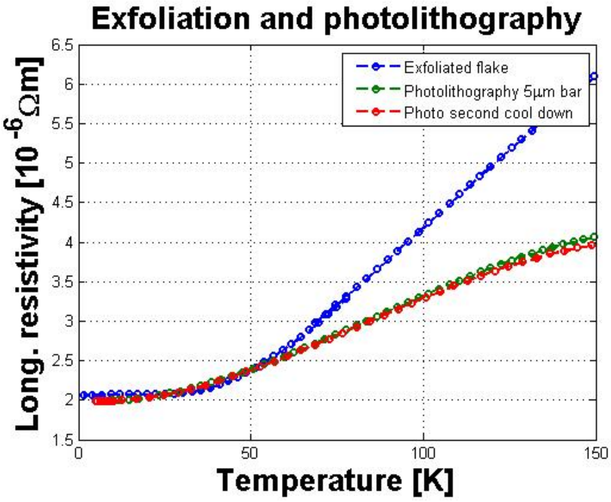

Figure 6.3: The longitudinal resistivity from two Hall bars with the same Bi_2Te_3 thin film was measured; one fabricated through exfoliation and one from direct patterning with photolithography. The Bi_2Te_3 thin film was grown on top of a semiconducting substrate, which contributes to the resistivity of the directly patterned device at high temperatures. At lower temperatures the resistivities approaches the same value.

length and width of the flake influenced the results. The length was relatively well defined for both the photolithography and exfoliation fabricated samples, and could be measured using optical microscope or the original AutoCAD drawing. Also, the width of the photolithography fabricated Hall bars was well defined. However, the width of the exfoliated topological insulator varied a lot on the same flake. The variation was up to 2 μm on 5-20 μm flakes, resulting in an uncertainty of 40 % of the width and hence of both the resistivity and mobility of the devices.

The resistivity of the devices was measured from room temperature down to 5 K. In Figure 6.3 only the lower part of the temperature dependence is shown. The Bi_2Te_3 thin films were mainly grown on top of silicon and undoped gallium arsenide substrates. When direct patterning was used on thin films grown on gallium arsenide substrates, the transport measurements had signatures of an extra conduction layer. At elevated temperatures the resistance appeared less than the true resistance and the carrier concentration appeared higher. This can be seen in Figure 6.3, where the longitudinal resistivity of the photolithography fabricated device is smaller than the resistivity of the device fabricated with exfoliation at temperatures down to 60 K.

Above 150 K the resistivity of the photolithography fabricated device decreased, implying another dominating type of conduction that could be due to the substrate. A conducting gallium arsenide sample at elevated temperatures could be an effect from the tellurium doping, since tellurium is an efficient n-type doping of gallium arsenide. Wang *et al* confirms an excess of tellurium when layer by layer growth was used, and claims that the excess of tellurium diffuses on the surface at higher growth temperatures. However, the conducting substrate should not influence the measurements at temperatures below 50 K, where the resistivity was similar according to Figure 6.3. Therefore the conduction through Bi_2Te_3 can be assumed to be dominating over the conducting gallium arsenide sample at low temperatures.

6.2 Proximity effect in Bi_2Te_3 and Bi_2Se_3

The Bi_2Te_3 thin films with the most promising results from the different growth processes were used in the proximity effect characterization, i.e. the thin film with a volume carrier concentration of 8.6 x 10^{20} cm^{-3} and a mobility of 220 cm^2/Vs from the first growth and the thin film with a volume carrier concentration of 4.4 x 10^{18} cm^{-3} and a mobility of 5500 cm^2/Vs from the second growth.

For all Josephson junctions and superconducting quantum interference devices, the superconducting coupling between the two aluminum electrodes was measured. The Josephson coupling was confirmed by radio-frequency and magnetic field measurements at temperatures around 300 mK. This can be seen in Figure 6.4 respectively 6.5. The temperature dependence of some junctions was also examined and is presented in the next section. Some devices were in addition measured at temperatures down to 20 mK.

6.2.1 Response to microwave radiation

To examine the response in electromagnetic field, an AC-voltage signal was applied over the Josephson junction, resulting in the current-voltage characteristics in Figure 6.4(a). The AC-voltage signal had a frequency of 1 GHz and varying amplitude power. The response of the current-voltage characteristics in the Josephson junctions was as expected from Chapter 2.3. When the power was increased to a certain value, -30 dbm in Figure 6.4(a), steps appeared in the current-voltage characteristics. Increasing the signal further, the response became more prominent, but disappeared at high power.

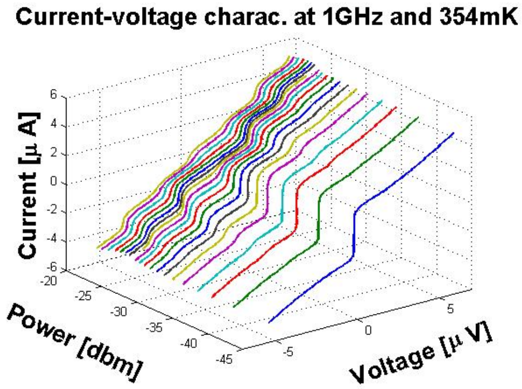

(a) IV curves in RF with different power.

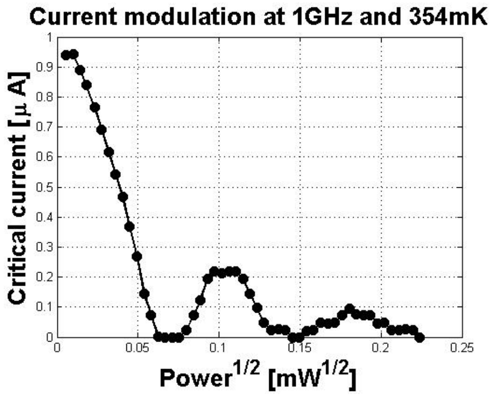

(b) Current as a function of RF power.

Figure 6.4: (a) Current-voltage characteristics was measured in 1 GHz with varying power of the signal. When the power was higher, steps in the IV-charachteristics appeared at $V_n = \frac{nh}{2e}f$. The size of the voltage steps was 1.6 μV. (b) The critical current modulated as a function of the power.

The distance between the steps were 2.1 μV for the measurement done at 1 GHz frequency in Figure 6.4(a). This is in agreement with 2 μV predicted from $\Delta V = \frac{h}{2e}f$. Measurements were also conducted at 1.7 GHz and 2.7 GHz with the resulting step distance of 3.2 μV and 5.7 μV respectively. This also corresponded well with the predicted values of 3.5 μV for 1.7 GHz and 5.6 μV for 2.7 GHz. Consequently, the voltage step position corresponded to integer Shapiro steps and scales with the frequency of the AC-voltage source.

In comparison to our results, a change in the voltage step behavior was found in hybrid InSb - Nb nanowire junctions [6]. In lower or no magnetic field the hybrid nanowires had voltage steps as for conventional Josephson junctions, but at high magnetic fields it was doubled to $V = \frac{hf}{e}$. In the conventional junctions the step originated from Cooper pairs tunneling with a charge of $2e$ as described in Chapter 2.3. The change to the double voltage step, suggests quasiparticle tunneling with a charge of e. This could be a signature of the Majorana zero modes. However, this was not observed in our measurements where the distance between the steps did not change for high magnetic fields.

The height of the steps ΔI modulated with the amplitude of the AC signal. The current was evaluated as a function of the square root of the amplitude of the signal, as in Figure 6.4(b), and was normalized with the critical current evaluated from the current-voltage measurements. There was a clear oscillatory behavior of the current when the power was increased. As expected for Josephson junctions, the amplitude of the measured current was maximum without microwave radiation and decreased as the power increased. The oscillations became damped when applying higher power.

6.2.2 Response to magnetic field

In Figure 6.5 the magnetic pattern of a Josephson junction (Figure 6.5(a)) and a SQUID (Figure 6.5(b)) is shown. The critical current of the Josephson junctions was 1-1.5 μA for junctions designed with an area of 0.2-0.5 μm^2. For teh SQUIDs the measured critical current was 0.05 μA for a deigned area of 25 μm^2.

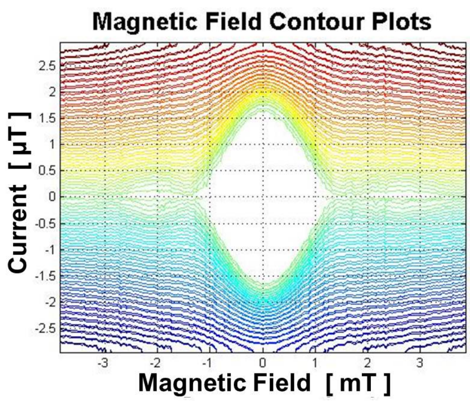

(a) Josephson junction.

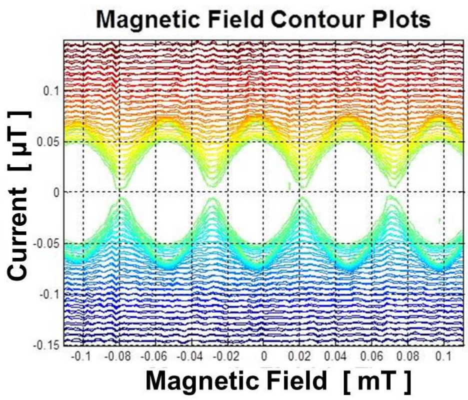

(b) SQUID.

Figure 6.5: (a) Current-voltage curves at 20 mK while scanning the magnetic field for a Josephson junction with 200 nm between the electrodes and (b) IV-curves at 20 mK for a SQUID with 250 nm between the electrodes.

In Figure 6.5(b) the SQUID's response to magnetic field showed critical current lobes of the same size, as predicted in Chapter 2.3.1. Comparing the magnetic response for the SQUID to the simulated Fraunhofer pattern in Figure 2.10 the behavior is similar.

The distance between the minimums of the lobes was 0.05 mT in Figure 6.5(b), which corresponds to a SQUID effective are of 34 μm^2. The measured effective area is slightly larger but in agreement with the designed area of 25 μm^2. Similar measured effective areas were found when measuring the the reference-SQUIDs. The slightly larger areas could be explained by leakage of superconductivity to the surrounding flake.

In comparison to the Josephson junctions, the magnetic pattern of the Josephson junction had one large lobe and then smaller, almost disappearing second lobes. The third lobes were not visible. The lobes reducing amplitude is slightly faster than the predictions of the Fraunhofer pattern in Figure 2.6.

Similar to our results, Yang et al. [7] showed patterns that do not deviate from the expected Fraunhofer pattern of a Josephson junction. However, the Fraunhofer pattern for Josephson junctions made by Williams *et al.* [9] found additional features for $I > I_c$. The additional features scaled with the magnetic field and the shape of the Frauhofer patter deviated from the expected. Our results did not have additional features, but the lobes decayed faster than the predicted Fraunhofer pattern. Williams et al. [9] had, in addition, noticed a critical field that was five times smaller than expected and a larger effective area.

6.2.3 Critical current temperature dependence

The resistance of some devices was measured as a function of temperature. A resistance drop appeared when the aluminum electrodes became superconducting at the critical temperature of around 1.1 K. There was also a smaller additional resistance drop at slightly lower temperature, indicating at which temperature the superconductivity was induced into the topological insulator. The critical temperature of the aluminum and the topological insulator varied a bit depending on the evaporation conditions and the defects in the films.

SQUID magnetic response dependence of temperature

The magnetic response of the SQUID was also examined at different temperatures and the results are presented in Figure 6.6. The SQUID modulated with the same period, independently of the temperature. The modulation of the SQUID was only dependent on the flux through the SQUID and hence the magnetic field.

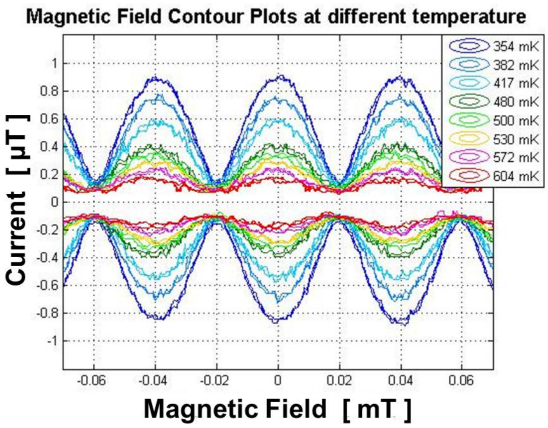

Figure 6.6: The current-voltage of the SQUID was measured as a function of the applied magnetic field at different temperatures. The modulation of the SQUID was independent of the temperature, while the amplitude of the lobes were decreasing with temperature as expected by simulations.

However, the amplitude of the lobes decreased with increasing temperature until the modulation was not observable above 850 mK. The amplitude of the lobes are determined by the critical current. Therefore the lobes followed the critical current dependence, which was as expected.

Critical current temperature dependence in Josephson junctions

In Figure 6.7 the measured current-voltage relation is presented for a Josephson junction at different temperatures. The measured critical current decreased when the temperature increased. At 1 K the Josephson junction made a transition from the superconducting state to the normal and above this temperature the junction behaved resistively. When decreasing temperature, the measured critical current increased as expected from the RSJ simulations in Chapter 2.3.3 and was in the range of 1-1.5 μA for the junctions.

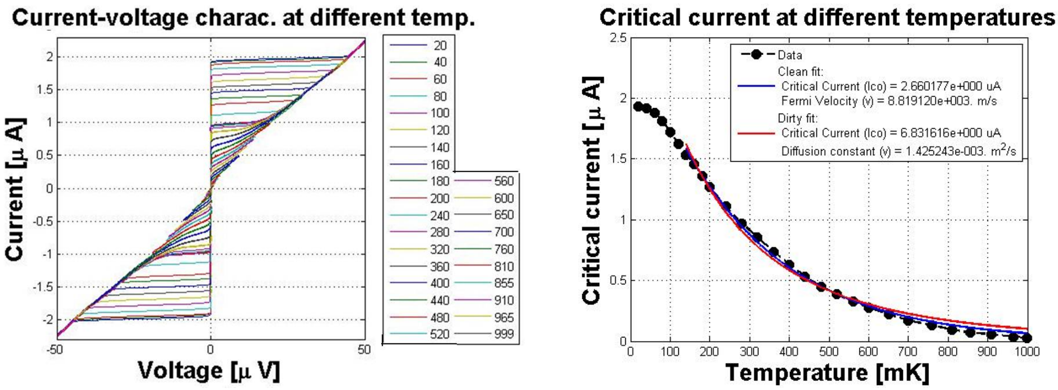

(a) IV curves at different temperatures.

(b) Fitting of the RSJ models.

Figure 6.7: IV curves at different temperatures for a Josephson junction with 200 nm between the electrodes. (a) The measured critical current increases with temperature and the response of the junction approaches the ideal case of a Josephson junction. (b) The critical current of the IV curves in (a) evaluated in the clean and the dirty limit. In the clean limit the Fermi velocity and critical current were calculated to 9 km/s and 2.7 μA. The critical current extracted from the dirty limit was 7 μA and the diffusion coefficient was 14 $^{\text{cm}^2}/_{\text{s}}$.

The data was evaluated in the clean and dirty limit according to

$$\begin{aligned} &\text{Clean limit } (l_n \gg \xi_{nc}) \text{ ; } I_c = I_{c0}e^{-L/L_0}, \text{ with } L_0 \approx \xi_{nc}(T) \\ &\text{Dirty limit } (l_n \ll \xi_{nd}) \text{ ; } I_c = \frac{A}{\xi_{nd}(T)}e^{-L/\xi_{nd}(T)} \end{aligned} \tag{6.1}$$

where l_n is the mean free path in topological insulator, ξ_{nc} and ξ_{nd} are the coherence lengths for a clean and dirty junction. The relation between the mean free path and coherence length determines if the junction is in the clean ($l_n \gg \xi_{nc}$) or dirty limit ($l_n \ll \xi_{nd}$).

Both the clean limit and dirty limit fits are shown together with the data in Figure 6.7(b). The data fits well to both limits. However, both models are only valid for temperatures where the coherence length is much larger than the distance between the electrodes [38]. This results in a restriction of the models; they are only valid above a certain temperature and can only be evaluated on data points above this. The coherence length and the distance between the electrodes were compared by simulations, showing that the clean limit and dirty limit models were valid above 150 mK.

According to the clean limit coherence length, the Fermi velocity could be extracted as $v_c = \frac{2\pi k_B T}{\hbar}\xi_{nd}$. The Fermi velocities for different devices and topological insulators are shown in Table 6.3 together with the results from the Hall measurements.

In the clean limit a Fermi velocity of 9 km/s was extracted from the same device as shown in Figure **??**. This value do not correspond to the around 400 km/s obtained from ARPES measurements [39, 40]. Similar results were presented in recently by Veldhorst [8], where the results were evaluated to be in the clean limit. However, our data seem to fit in both the dirty and clean limit.

In the dirty regime, the diffusion coefficient could be evaluated through $D_n = \frac{2\pi k_B T}{\hbar}\xi_{nd}$ and was extracted from the data in Figure 6.7 to a value of 14 cm^2/s. This suggests that the conduction was dependent on the scattering of impurities.

The junction in Figure 6.7 had 200 nm between the electrodes and was fabricated with Bi_2Te_3 thin film from the second growth process. Similar results were achieved with a 150 nm junction on the same sample. As presented in table 6.3, this sample had two order of magnitude lower carrier concentration and twenty times higher mobility than the best sample from the first growth process. Despite the large improvement in carrier concentration and mobility, both the clean Fermi velocity and dirty limit diffusion coefficient were of similar value. However, the evaluated critical current for the first growth process sample was higher. When evaluating the data in the clean and dirty limit, the value of the critical current depended a lot on how the threshold was set. Therefore, this deviation could be due to the instability of critical current in the models.

Both the Fermi velocity and the diffusion coefficients for the Bi_2Te_3 junctions were in the same order of magnitude as for the Bi_2Se_3 junction of 400 nm. The Bi_2Se_3 samples had in general higher mobility and lower carrier concentration than the thin films in the first growth process. During the second growth processes the thin films improved and had comparable results to the Bi_2Se_3 single crystal. One sample from the second growth process of Bi_2Te_3 thin films had comparable mobility and a lower carrier concentration than the Bi_2Se_3 samples. However, despite these transport properties the Bi_2Te_3 sample did not indicate oscillations in the Hall measurements.

6.3 Topography and spectroscopy

In addition to transport measurements, the Bi_2Te_3 thin film with highest mobility and lowest carrier concentration was characterized in a scanning tunneling microscope described in 5.2. Using the scanning tunneling microscope, the need of a clean surface is more crucial than in transport measurements. Therefore the samples were cleaved, manipulated and measured *in situ*.

The topography of the Bi_2Te_3 thin film presented in Figure 6.8(a) was taken with a bias current of 0.04 nA and voltage +0.4 V at 300 mK. The brighter parts on the surface are terraces, which are flakes with more layers that the base of the film. An approximation from a line cut in the topography image showed a terrace height of 4 Å to 6 Å, confirming a roughness of the Bi_2Te_3 films even after the cleaving. The topology profile is shown in Figure 6.9(b) and describes the height depending on the position along the line. The green line cut describes three different terraces on top of the base, while the blue line in addition shows that the base has 8 Å thick layers on top of another

Table 6.3: Carrier concentration and mobility calculated from Hall measurements, together with critical current, Fermi velocities and diffusion coefficients extracted from fitting the RSJ model in the clean and dirty limit to the temperature dependent proximity effect measurements. Two Josephson junctions with different widths were measured for the best Bi_2Te_3 sample and the corresponding parameters are in the same column.

Properties	Bi_2Te_3 1^{st} growth process	Bi_2Te_3 2^{nd} growth process		Bi_2Se_3 single crystal
Flake thickness	75 nm	80 nm		90 nm
Carrier concentration	$8.6 \times 10^{20}\,\mathrm{cm}^{-3}$	$4.4 \times 10^{18}\,\mathrm{cm}^{-3}$		$1.3 \times 10^{19}\,\mathrm{cm}^{-3}$
Mobility	$220\,\mathrm{cm^2/Vs}$	$5500\,\mathrm{cm^2/Vs}$		$5100\,\mathrm{cm^2/Vs}$
Width of electrodes	$2\,\mu$m	$2\,\mu$m		$2\,\mu$m
Distance between electrodes	250 nm	150 nm	200 nm	400 nm
Clean limit Fermi velocity	$4\,\mathrm{km/s}$	$7\,\mathrm{km/s}$	$9\,\mathrm{km/s}$	$10\,\mathrm{km/s}$
Clean limit critical current	$27\,\mu$A	$1.3\,\mu$A	$2.7\,\mu$A	$6\,\mu$A
Dirty limit critical current	$880\,\mu$A	$4.6\,\mu$A	$8.0\,\mu$A	$45\,\mu$A
Dirty limit diffusion coefficient	$5\,\mathrm{cm^2/s}$	$20\,\mathrm{cm^2/s}$	$29\,\mathrm{cm^2/s}$	$34\,\mathrm{cm^2/s}$

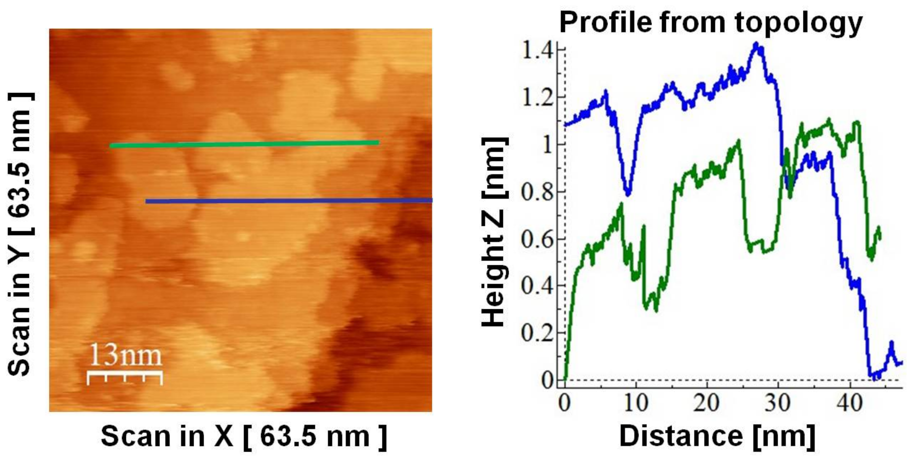

(a) Topography of Bi_2Te_3.

(b) Profile of topography.

Figure 6.8: A scanning tunneling microscope was used on the Bi_2Te_3 thin film with highest mobility and lowest carrier concentration. (a) The topography shows terrace like islands. (b) Across the line in (a) the height was evaluated according to position. The islands have a height of 4-6 nm.

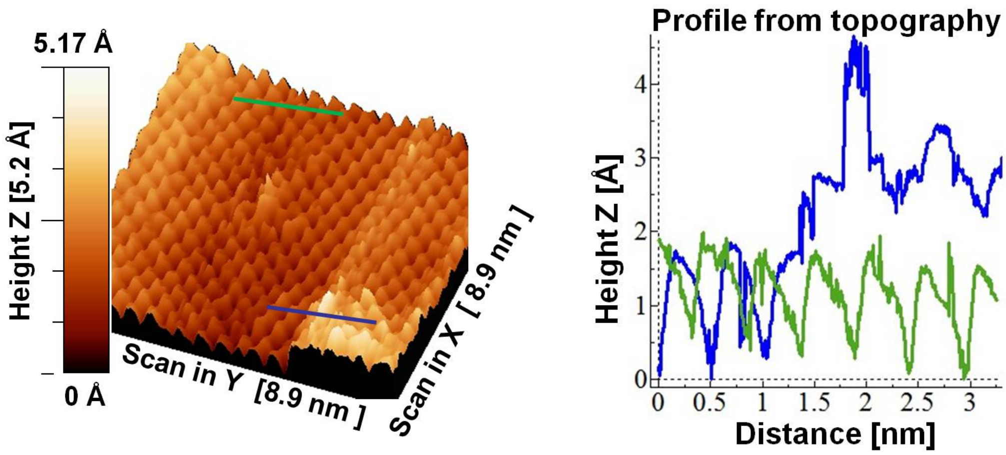

(a) Topography of Bi_2Te_3.

(b) Profile of topography.

Figure 6.9: The Bi_2Te_3 sample with the highest mobility and lowest carrier concentration was measured in the scanning tunneling microscope. (a) Close to atomic resolution showed hexagonal crystalline structure with (b) an ion size of almost 1.5 Å according to the green line cut. The blue line, cut a step with the height 3 Å corresponding to two atomic layers.

thin film base. This indicates a layered material with a relatively large roughness on a larger scan area.

A higher resolution topology image was taken, showing almost atomic resolution in Figure 6.9(a). Height of the image describes the electronic distribution on the surface, where the larger peaks most probably are due to defects in the layers closest to the surface. A profile of the topology is shown in Figure 6.9(b). The green line is a line cut from a peak in the electronic distribution, through six atoms to the last one. Each peak

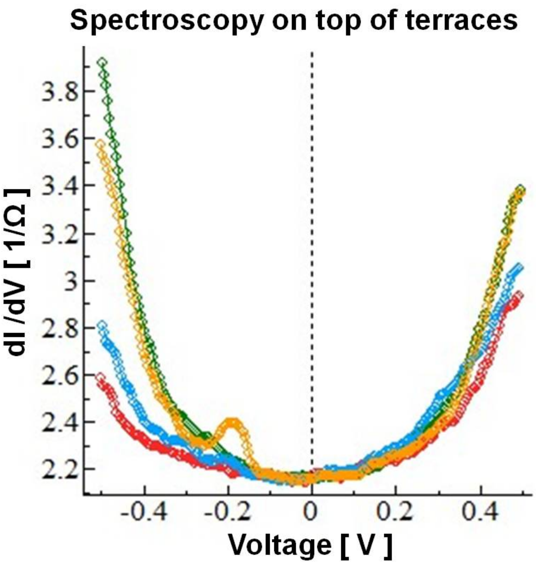

Figure 6.10: Spectroscopy was evaluated at different positions, both on top of terraces and on the base. The curves have the same behavior and were taken with bias current 0.04 nA and voltage +0.4 V. The spectroscopy was taken from +0.5 V to -0.5 V or -0.6 V.

in the conductance spectra give rise to a height around 1.5 Å. The blue line describes a double step of 3 Å up to the brighter part in Figure 6.9(a). On top of this step, there is another feature, which is most probably due to noise in the system when the tip had to adjust for a larger height difference.

Spectroscopy was only taken on top of different terraces, due to lack of stability on the base film. The spectra in Figure 6.10 was obtained using a standard lock-in technique with 0.5 mV bias modulation. The spectra were taken from +0.5 V to -0.5 V with a current set-point of 40 pA and are somewhat noisy and not clear. However, a Dirac cone was indicated at around 200 mV. The position of the Dirac cone depends on the chemistry of the sample, but is similar to the 200 mV found by Chen *et al* [41], 335 meV found by Alpichshev *et al* [42] and 340 meV found by Wang *et al* [36].

Similarly to the expected oscillations at high field during Hall measurements, the Landau levels should appear as peaks in the scanning tunneling microscope spectra and has been observed in topological insulators at 7 T magnetic field [43]. Our Bi_2Te_3 thin film was measured at a magnetic field of the same strength at a lower temperature, but no oscillations were found. However, the oscillations might occur at higher magnetic field in our sample due to a different chemical composition. Unfortunately this could not be investigated further due to limitations in strength of the superconducting magnetic. The Shubnikov-de Haas oscillations were also observed by Yu *et al* [37], where MBE grown Bi_2Te_3 thin films were measured at magnetic fields up to 9 T at 1.9 K. The top and bottom surface conduction could be separated with different oscillatory frequencies by electronically gating the top surface.

6.4 Proximity effect by nanodots

The fabrication of nano-sized dots gave hexagonal dots in patterns with distances down to 200 nm. For a distance of 100 nm, the lift-off did not work and the whole aluminum sheet was left on top of the topological insulator. The measurements of devices with nanodot distances from 200 nm to 800 nm showed a resistance with a metallic temperature behavior. This means that the nanodots did not induce superconductivity well enough to measure the signatures of it, which is most probably due to a bad interface between the dots and the topological insulator. A large roughness of the film could affect the contact area of the dot and also induce a large inhomogeneity in the pattern. In addition the previous fabrication steps could have left residues on top of the topological insulator, increasing the bad contact.

To improve the interface I suggest that the dots are put on a newly cleaved topological insulator film. This could be done in a scanning tunneling microscope with a build in evaporative system. Another possibility is to put the topological insulator on top of prepatterned electrodes and fabricate the dots directly afterward. In this way the number of fabrication steps on the topological insulators is decreased, which might result in less resist residues and contamination on the topological insulator surface.

7

Conclusion

THE PROPERTIES OF THE 3D TOPOLOGICAL INSULATORS Bi_2Te_3 and Bi_2Se_3 have been investigated by theoretical studies, cleanroom fabrication, surface inspection and transport measurements. The transport properties of Bi_2Te_3 and Bi_2Se_3 have been characterized by measurements of fabricated Hall bars, Josephson junctions and superconducting quantum interference devices. The results were similar to simulations and previous work within the research field.

The Hall measurements performed on Bi_2Te_3 showed a negative Hall constant, indicating n-type charge carriers dominating the transport. During the Bi_2Te_3 growth an improvement from $1\text{x}10^{21}\,\text{cm}^3$ to $4.4\text{x}10^{18}\,\text{cm}^8$ in the carrier concentration and from $150\,\text{cm}^2/\text{Vs}$ to $5500\,\text{cm}^2/\text{Vs}$ in the mobility was shown. This means that the Bi_2Te_3 growth could be optimized to have comparable transport properties to the Bi_2Se_3 single crystal, with a carrier concentration of typically $1.3 \text{ x } 10^{19}\,\text{cm}^3$ and mobility of typically $5100\,\text{cm}^2/\text{Vs}$. However, none of the Bi_2Te_3 devices showed Shubnikov-de Haas oscillations, as observed in Bi_2Se_3.

The samples with the lowest carrier concentration and the highest mobility from the three different growth processes were further characterized in Josephson junctions and superconducting quantum interference devices, SQUIDs. The Josephson coupling in these devices was confirmed by their response in microwave radiation and magnetic field at around 300 mK and 20 mK. When a radio-frequency AC signal was applied over the junctions, integer Shapiro steps were observed. The width of the steps in voltage varied depending on the radio-frequency of the AC signal as $\Delta V = \frac{h}{2e}f$.

From the magnetic response of the Josephson junctions and SQUIDs, the Fraunhofer patterns were as expected. The critical current in the Josephson junctions was 1-2 μA depending on the junction area, which was ranging from $0.1\,\mu\text{m}^2$ to $1\,\mu\text{m}^2$. The SQUIDs had a critical current of $0.05\,\mu$A for designed area of $25\,\mu\text{m}^2$, while the modulation of the SQUID represented an area of $34\,\mu\text{m}^2$. Both the area and the magnetic response is similar to the the reference SQUIDs without the topological insulator weak link.

In addition to the response to microwave radiation and to magnetic field, the temperature dependence of the Josephson junction was evaluated and fitted in the clean and dirty approximation. For the Bi_2Te_3 thin film with the highest carrier concentration and lowest mobility, the clean limit gave a Fermi velocity of $9\,\text{km}/\text{s}$. This was similar $10\,\text{km}/\text{s}$ for the Bi_2Se_3 single crystal. Neither of the velocities corresponded to the values obtained from ARPES measurements [39, 40]. From the dirty limit fittings the diffusion constant was extracted to $29\,\mathrm{cm^2/s}$ for the Bi_2Te_3 sample and $34\,\mathrm{cm^2/s}$ for the Bi_2Se_3.

The Bi_2Te_3 thin film with lowest carrier concentration and mobility was further characterized in a scanning tunneling microscope. The topography and spectrscopy showed a roughness of 3 Å on top of 6 Å thick flakes on top of the thin film base. During the spectroscopy a Dirac cone was indicated at 200 mV, similar to previous research results [36, 41, 42].

7.1 Work prospects

A continuation of the Bi_2Te_3 growth should focus on less rough thin films, using a growth temperature of 180 °C and tellurium bismuth flux ratio of 130 . The thin film should be grown on smooth non-conductive substrate to enable direct fabrication and smoother films. If oscillations are observed, the oscillations should be investigated as a function of the angle between the surface of the sample and the magnetic field. Since the magnetic field only effects the surface perpendicular to it, this would be a way to distinguish the surface from the bulk.

In addition to the angle dependent magnetic Hall measurements, doping could be used to isolate the surface from the bulk. Chemical doping has been done on Bi_2Se_3 where the bulk conductivity can be disregarded by electrolyte back gate doping [44]. Since Bi_2Te_3 and Bi_2Se_3 are more sensitive to applied fields than semi-conductors [11], their carrier density should be modified by electro-doping [45]. Electromagnetic field doping is of special interest since it is easy to tune and not permanent as chemical doping.

As a side project during this thesis, I investigated electromagnetic field doping as described in Appendix C.1. Three different designs were considered for the electro-gating; gating from the top, from the sides and from below. Both the top and coplanar gate seemed to influence the samples, but the effect could also have been due to the electrolyte reacting with the sample [46]. A clear drift in resistance was shown over the timescale of an hour. The bottom gate was realized, but required a lot of effort to place the flakes on top of the pre-patterned substrate. In addition, the precision of the electrodes had to be exact and could so far not be realized. This design should be further developed since it seems promising. However, a requirement for the doping is low carrier concentration and should therefore be tried on thin films from the second growth process. On these topological insulators new experiments with coplanar gating could also be done, but then with purely electronic proximity gating.

In the last three month of the thesis project I designed a new layout with dots on top of the topological insulators. This is interesting to examine since the superconductivity is induced between all the nanodots to the topological insulators surface. This would be a way to realize 2D superconductivity and was done with niobium nanodots on top of a gold thin film [33]. This side project required two more electron lithography steps and was later realized with photolithography, but still required an additional electron beam lithography step in the fabrication. The dimensions of the design were chosen from the experience gained during the thesis work on Josephson junctions and the same materials were use. One difficulty was to get the interface clean enough between the nanodots and the topological insulator.

Bibliography

[1] J. E. Moore, The birth of topological insulators, Nature 464 (2010) 194.

[2] H. C. Manoharan, A romance with many dimensions, Nat. Nanotechnol. 5 (2010) 477.

[3] N. Seizo, The crystal structure of $Bi_2Te_{3-x}Se_x$, J. Phys. Chem. Solids 24 (1963) 479.

[4] H. Peng, K. Lai, D. Kong, S. Meister, Y. Chen, X.-L. Qi, S.-C. Zhang, Z.-X. Shen, Y. Cui, Aharonov-Bohm interference in topological insulator nanoribbons, Nat. Mater. 9 (2009) 225.

[5] D. Zhang, J. Wang, A. M. DaSilva, J. S. Lee, H. R. Gutierrez, M. H. W. Chan, J. Jain, N. Samarth, Superconducting proximity effect and possible evidence for Pearl vortices in a candidate topological insulator, Phys. Rev. B 84 (2011) 165120.

[6] L. P. Rokhinson, X. Liu, J. K. Furdyna, The fractional a.c. Josephson effect in a semiconductor-superconductor nanowire as a signature of Majorana particles, Nat. Phys. 8 (2012) 795.

[7] F. Qu, F. Yang, J. Shen, Y. Ding, J. Chen, Z. Ji, G. Liu, J. Fan, X. Jing, C. Yang, L. Lu, Strong Superconducting Proximity Effect in Pb-Bi_2Te_3 Hybrid Structures, Sci. Rep. 2 (2011) 389.

[8] M. Veldhorst, M. Snelder, M. Hoek, T. Gang, V. K. Guduru, X. L. Wang, U. Zeitler, W. G. van der Wiel, A. A. Golubov, H. Hilgenkamp, A. Brinkman, Josephson supercurrent through a topological insulator surface state, Nat. Mat. 11 (2012) 417.

[9] J. R. Williams, A. J. Bestwick, P. Gallagher, S. S. Hong, Y. Cui, A. S. Bleich, J. G. Analytis, I. R. Fisher, D. Goldhaber-Gordon, Unconventional Josephson Effect in Hybrid Superconductor-Topological Insulator Devices, Physical Review Letters 109 (5) (2012) 056803.

[10] J. E. Moore, Topological insulators: The next generation, Nat. Phys. 5 (2009) 378.

[11] J. E. Moore, Topological Insulators, IEEE Spectrum 48 (2011) 38.

[12] Y. L. Chen, J. G. Analytis, J.-H. Chu, Z. K. Liu, S.-K. Mo, X. L. Qi, H. J. Zhang, D. H. Lu, X. Dai, Z. Fang, S. C. Zhang, I. R. Fisher, Z. Hussain, Z.-X. Shen,

Experimental Realization of a Three-Dimensional Topological Insulator, Bi_2Te_3, Science 325 (2009) 178.

[13] F. Liang, C. Kane, Superconducting Proximity Effect and Majorana Fermions at the Surface of a Topological Insulator, Phys. Rev. Lett. 100 (2008) 096407.

[14] H. Zhang, C. Liu, X. Dai, Z. Fang, S. Zhang, Topological insulators in Bi_2Se_3, Bi_2Te_3 and Sb_2Te_3 with a single Dirac cone on the surface, Nat. Phys. 5 (2009) 438.

[15] X. Chen, H. D. Zhou, A. Kiswandhi, I. Miotkowski, Y. P. Chen, P. A. Sharma, A. L. L. Sharma, M. A. Hekmaty, D. Smirnov, Z. Jiang, Thermal expansion coefficients of Bi_2Se_3 and Sb_2Te_3 crystals from 10 K to 270 K, Appl. Phys. Lett. 99 (2011) 261912.

[16] M. Franz, Majorana's wires, Nat. Nanotechnol. 8 (2013) 149.

[17] D. Teweldebrhan, V. Goyal, A. A. Balandin, Exfoliation and Characterization of Bismuth Telluride Atomic Quintuples and Quasi-Two-Dimensional Crystals, Nano Letters 10 (2010) 1209.

[18] X. Qi, S. Zhang, The quantum spin Hall effect and topological insulators, Physics Today 63 (2010) 33.

[19] W. Zhang, R. Yu, H.-J. Zhang, X. Dai, Z. Fang, First-principles studies of the three-dimensional strong topological insulators Bi_2Se_3, Bi_2Te_3 and Sb_2Te_3, New J. Phys. 12 (2010) 065013.

[20] C. Beenakker, Search for Majorana fermions in superconductors, Annu. Rev. Con. Mat. Phys. 4 (1) (2013) 113.

[21] J. Alicea, New directions in the pursuit of Majorana fermions in solid state systems, Rep. Prog. Phys. 75 (2012) 076501.

[22] F. Duan, J. Guojun, Introduction to Condensed Matter Physics, World Scientific Publishing, Singapore, 2005.

[23] K. von Klitzing, Nobel lecture: The Quantized Hall Effect (December 1985).

[24] M. König, S. Wiedmann, C. Brüne, A. Roth, H. Buhmann, L. W. Molenkamp, X.-L. Qi, S.-C. Zhang, Quantum Spin Hall Insulator State in HgTe Quantum Wells, Science 318 (2007) 766.

[25] A. Barone, G. Paterno, Physics and Applications of the Josephson Effect, John Wiley and Sons, United States of America, 1982.

[26] J. R. Waldram, Superconductivity of Metals and Cuprates, CRC Press, 1996.

[27] F. London, H. London, The Electromagnetic Equations of the Supraconductor, Proceedings of the Royal Society of London. Series A, Mathematical and Physical Sciences 149 (1935) 71.

[28] M. Leijnse, K. Flensberg, Introduction to topological superconductivity and Majorana fermions, Semicond. Sci. Technol. 27 (2012) 124003.

[29] R. M. Wilson, Evidence for Majorana fermions in a nanowire, Physics Today 265 (2012) 14.

[30] A. Kitaev, Unpaired Majorana fermions in quantum wires, Phys. Usp. 44 (131).

[31] A. Das, Y. Ronen, Y. Most, Y. Oreg, M. Heiblum, H. Shtrikman, Zero-bias peaks and splitting in an Al-InAs nanowire topological superconductor as a signature of Majorana fermions, Nat. Phys. 8 (2012) 887.

[32] L. Jiang, D. Pekker, J. Alicea, G. Refael, Y. Oreg, F. von Oppen, Unconventional Josephson signatures of Majorana bound states., Phys. Rev. Lett. 107 (2011) 236401.

[33] S. Eley, S. Gopalakrishnan, P. M. Goldbart, N. Mason, Approaching zero-temperature metallic states in mesoscopic superconductor–normal–superconductor arrays, Nat. Phys. 8 (2011) 59.

[34] C. Nordling, J. Österman, Physics Handbook for Science and Engineering, Studentlitteratur, Poland, 2006.

[35] C. B. Satterthwaite, R. W. Ure, Electrical and Thermal Properties of Bi_2 Te_3, Phys. Rev. 108 (1957) 1164.

[36] G. Wang, X.-G. Zhu, Y.-Y. Sun, Y.-Y. Li, T. Zhang, J. Wen, X. Chen, K. He, L.-L. Wang, X.-C. Ma, J.-F. Jia, S. B. Zhang, Q.-K. Xue, Topological Insulator thin Films of Bi_2Te_3 with Controlled Electronic Structure, Adv. Mater. 23 (2011) 2929.

[37] X. Yu, L. He, M. Lang, W. Jiang, F. Xiu, Z. Liao, Y. Wang, X. Kou, P. Zhang, J. Tang, G. Huang, J. Zou, K. L. Wang, Separation of top and bottom surface conduction in Bi_2Te_3 thin films, Nanotechnology 24 (2013) 015705.

[38] K. K. Likharev, Superconducting weak links, Rev. Mod. Phys. 51 (1979) 101.

[39] Y.-Y. Li, G. Wang, X.-G. Zhu, M.-H. Liu, C. Ye, X. Chen, Y.-Y. Wang, K. He, L.-L. Wang, X.-C. Ma, H.-J. Zhang, X. Dai, Z. Fang, X.-C. Xie, Y. Liu, X.-L. Qi, J.-F. Jia, S.-C. Zhang, Q.-K. Xue, Intrinsic Topological Insulator Bi_2Te_3 Thin Films on Si and Their Thickness Limit, Adv. Mater. 22 (2010) 4002.

[40] L. Plucinski, G. Mussler, J. Krumrain, A. Herdt, S. Suga, D. Grützmacher, C. M. Schneider, Robust surface electronic properties of topological insulators: Bi_2Te_3 films grown by molecular beam epitaxy, Appl. Phys. Lett. 98 (2011) 222503.

[41] M. Chen, J.-P. Peng, H.-M. Zhang, L.-L. Wang, K. He, X.-C. Ma, Q.-K. Xue, Molecular beam epitaxy of bilayer Bi(111) films on topological insulator Bi_2Te_3: A scanning tunneling microscopy study, Appl. Phys. Lett. 101 (2012) 081603–1.

[42] Z. Alpichshev, J. Analytis, J.-H. Chu, I. Fisher, Y. Chen, Z. Shen, A. Fang, A. Kapitulnik, STM Imaging of Electronic Waves on the Surface of Bi_2Te_3: Topologically Protected Surface States and Hexagonal Wraping Effects, Phys. Rev. Lett. 104 (2010) 016401–1.

[43] Y. Okada, W. Zhou, C. Dhital, D. Walkup, Y. Ran, Z. Wang, S. D. Wilson, V. Madhavan, Visualizing Landau Levels of Dirac Electrons in a One-Dimensional Potential, Phys. Rev. Lett. 109 (2012) 166407.

[44] D. Kim, S. Cho, N. P. Butch, P. Syers, K. Kirshenbaum, S. Adam, J. Paglione, M. S. Fuhrer, Surface conduction of topological Dirac electrons in bulk insulating Bi_2Se_3, Nat. Phys. 8 (2012) 460.

[45] D. Kong, W. Dang, J. J. Cha, H. Li, S. Meister, H. Peng, Z. Liu, Y. Cui, Few-Layer Nanoplates of Bi_2Te_3 and Bi_2Se_3 with Highly Tunable Chemical Potential, Nano Lett. 10 (2010) 2245.

[46] A. S. Dhoot, S. C. Wimbush, T. Benseman, J. L. MacManus-Driscoll, J. Cooper, R. H. Friend, Increased T_c in Electrolyte-Gated Cuprates, Adv. Mater. 22 (2010) 2529.

[47] E. Majorana, Theory of the Symmetry of Electrons and Positrons, Nuovo Cim. 14 (1937) 171.

A

Fabrication recipes

	Recipe for Bi_2Te_3 and Bi_2Se_3: exfoliation process	
	Fabrication step	Specifications
1	Spin protecting resist if Bi_2Te_3 thin film wafer	
	Dicing if Bi_2Te_3 thin film wafer and remove resist	
2	Exfoliation to get TI flakes on pre-patterned substrates	
3	AFM on TI flakes to get thickness	
4	Microscope pictures of flakes for AutoCAD	
5	AutoCAD mask making according to flakes' position	
6	Spinning of resist	PMMA EL 8 (10) at 5000 rpm (6000 rpm) for 1,5 min with 3 sec acc
	Baking of resist	135°C for 10 min
	Spinning of resist	ZEP 1:2 6000 rpm for 1,5 min with 3 sec acc
	Baking of resist	135°C for 10 min
7	Ebeam exposure	Junctions and contact pads
8	Developement	Hexylacetate for 33 sec, MIBK:IPA 1:1 for 2 min (3 min 45 sec)
9	Plasma etching	Ash 3 sec at 50W
10	Argon milling	V=300V, I=5μA, gas channel 4mL/min for 10 sec
11	Evaporation	Ti (5nm) or Pt (3nm) and Al (100nm) or Au (100nm)
12	Liftoff	Acetone bath at 50°C

Recipe for Bi_2Te_3: direct patterning with ebeam

	Fabrication step	Specifications
0	AutoCAD mask making	Same mask used repeatedly
1	Spin protecting resist on Bi_2Te_3 thin film wafer	
	Dicing Bi_2Te_3 thin film wafer and remove resist	
2	Spinning of resist	EL10 at 6000 rpm for 1,5 min with 3 sec acc
	Baking of resist	135°C for 10 min
	Spinning of resist	ZEP 1:2 6000 rpm for 1,5 min with 3 sec acc
	Baking of resist	135°C for 10 min
3	Ebeam exposure	Alignment crosses and reference marks
4	Developement	Hexylacetate for 33 sec, MIBK:IPA 1:1 for 3 min 45 sec
5	Plasma etching	Ash 3 sec at 50W
6	Argon milling	V=300V, I=5μA, gas channel 4mL/min for 10 sec
7	Evaporation	Ti (5nm) or Pt (3nm) and Al (100nm) or Au (100nm)
8	Liftoff	Acetone bath at 50°C
9	Spinning of resist	maN2401 at 3000 rpm for 30 sec with 0.5 sec acc
	Baking of resist	90°C for 1 min
10	Ebeam exposure	Topological insultor areas
8	Developement	MF24A for 1 min
9	Plasma etching	Ash 3 sec at 50W
10	Argon milling	V=300V, I=5μA, gas channel 4mL/min for 10 min
11	Cleaning	Acetone bath at 50°C
12	Repeat step 2	with PMMA EL 8 at 5000 rpm instead of EL10 at 6000 rpm
13	Ebeam exposure	Junctions and contact pads
14	Developement	Hexylacetate for 33 sec, MIBK:IPA 1:1 for 2 min
15	Repeat step 5-8	

Recipe for Bi_2Te_3: photolithography process

	Fabrication step	Specifications
1	Spin protecting resist on Bi_2Te_3 thin film wafer	
	Dicing Bi_2Te_3 thin film wafer and remove resist	
2	Dehydration baking	115°C for 5 min
	Spinning of primer	HDMS primer at 6000 rpm for 20 sec with 1 sec acc
	Spinning of resist	SPR220 6000 rpm for 1 min with 1 sec acc
	Baking of resist	90°C for 5 min
3	Photolithography	Expose edges for 50 sec
4	Developement	MF 4A for 20 sec and rince in DI water
5	Photolithography	Exposer TI areas for 10 sec
6	Developement	MF 4A for 40 sec and rince in DI water
7	Plasma etching	Ash 30 sec at 50W
8	Argon milling	V=300V, I=5μA, gas channel 4mL/min for 10 min
9	Cleaning	Acetone bath at 50°C
10	Repeat step 2-4	
11	Photolithography	Expose electrodes for 10 sec
12	Developement	MF4A for 50 sec and rince in DI water
13	Plasma etching	Ash 30 sec at 50W
14	Argon milling	V=300V, I=5μA, gas channel 4mL/min for 10 min
15	Evaporation	Ti (5nm) and Au (100nm)
16	Liftoff	Acetone bath at 50°C

B

Supplementary theory

B.1 Topological equivalence

In a normal insulator the valence band and conduction band are separated by a well defined energy gap. This gap is much larger in an insulator than in a semiconductor and the Fermi level lies between the minimum of the conduction band and the maximum of the valence band.

Interpolating between the insulating state and the semiconducting state without closing the energy gap can be done by tuning the Hamiltonian. This process defines a topological equivalence. The conventional insulators are equivalent to the vacuum, which has an energy gap between the conduction band of electrons and the valence band of positrons. However, there are insulating states that are not topologically equivalent with the vacuum. One example is the quantum Hall state that can be found in a topological insulator [2, 14].

B.2 Topological twist

To understand the band inversion, a model was suggested by Zhang *et al.* [14]. They studied the atomic levels with consideration of crystal-field splitting and spin orbit coupling. Using this model the twist of the topological insulator will be explained here. The electron configuration for the unfilled atomic levels is $6s^2 6p^3$ in bismuth, $4s^2 4p^4$ in selenium, and $5s^2 5p^4$ in tellurium. Near the Fermi surface the p-orbitals mainly contributes to the energy levels and the effect of the s-orbitals can be neglected.

The bismuth and selenium atomic states are hybridized when chemically bonded and the orbitals are combined according to their parity in a single unit cell within a quintuple layer. When considering the effect of crystal-field splitting between different p-orbitals, the p_z-orbitals split up from the degenerated p_x- and p_y-orbitals. Accordingly the hybridized states P_z and $P_{x,y}$ also split up. The hybridized P_z levels are pushed towards the Fermi level, while the other are pushed away from it [14].

The spin orbital coupling couples the spin and the orbitals, but preserves the total angular momentum. This results in a further repulsion between the P_z and $P_{x,y}$ levels, leading to a lowering of the P_z level from bismuth and a rising of the P_z level from selenium. Since the spin coupling is large in Bi_2Se_3 and Bi_2Te_3, the repulsion is large enough to reverse the energy order of the levels [14].

The parity of these levels is opposite, which means that the inversion exchanges the parity of the system driving it into a topological insulator phase shift of π [20]. In this topological phase the spin-orbit coupling has led to antisymmetric states with higher energy than symmetric states in certain regions. The shift of states antisymmetric and symmetric states can be seen as the twist in the band structure. This twist or cross over of conduction and valence band forms a Dirac cone on the surface [14] and can be seen as the red dotted lines in Figure 2.1 originating from the surface. If the bands cross over equally many times, there is an even number of Dirac cones on the surface. This is the case in for instance graphene. If the bands cross over an odd number of times it describes the topological insulator with an odd number of Dirac cones on the surface, like for Bi_2Te_3 and Bi_2Se_3.

B.3 Majorana excitations

When a topological insulator is used as the barrier in Josephson junctions and SQUIDs, Majorana particles can emerge as zero modes at the interfaces between the topological insulator and the superconductors. The requirements to produce Majorana particles may be met by using a superconductor where the spin-rotation and time-reversal symmetries are broken. This removes the degeneracies of the linear energy dispersion. In addition the gap should be closed and reopened, then the Majorana particles emerge as zero modes when the gap goes to zero.

When a strictly real-valued solution to the Dirac equation was found by Ettore Majorana in 1937 [47] it was in the field of particle physics. Seventy years later the nanoscientists and condensed matter physicists started focusing on Majorana particles, described by these solutions. A large interest has risen on explaining and finding these particles, especially Majorna particles occurring at exactly zero energy because they are their own antiparticles.

The Majorana particles are predicted to appear in the ends of quantum wires or at the interfaces between topological and non-topological regions of the wire. So far the Majorana particles have not been isolated, however signatures of Majorana particles have been reported [31].

Under certain conditions an ordinary fermion, like the electron, can be composed of a superposition of two Majorana particles [29]. Majorana particles are non-abelian anyons. This mean that they do not follow the normal statistics as for bosons or fermions and that their exchange operators do not commute in an ordinary way. In the non-abelian statistics the ground state is degenerated and separated from the excited states by a gap [28]. The requirement of a gap motivates the use of superconductivity [20] but there are more criteria for the Majorana particles to appear.

The Majorana zero modes exists under the certain condition that the ground state is degenerated [20], which means that electrons with same spin can pair up. This does not appear in normal s-wave superconductors, but is allowed in p-wave superconductivity [29]. However, p-wave superconductors rarely exists in nature and are very sensitive to disorder [28]. Artificial p-wave superconductors have been constructed with s-wave superconductors in proximity to a material with strong spin-orbit coupling. The tunneling Cooper pairs inherit the superconductivity from the superconductor and are phase shifted by the material with strong spin-orbit coupling. The Majorana particles then appear in the interfaces between the conventional superconductor and the material with strong spin-orbit coupling. These interfaces can be made through Josephson junction as described earlier in this chapter.

To be able to measure the signatures of a Majorana particle and not just the ordinary fermion, a single Majorana particle has to be spatially separated from the other. Otherwise, it will pair up with another Majorana particle and appear as an ordinary fermion. A model to understand this was proposed by Kitaev [30] with a one dimensional quantum wire subjected to p-wave superconductive pairing. The quantum wire can be described by a tight-binding chain, where the spinless electrons are hopping between the sites in the chain.

Each electron in the chain can be seen as a composition of two Majorana particles. In the Kitaev chain the Majorana particles can pair up in two ways; with the other Majorana particle in same site of the chain or with another Majorana particle in a neighboring site. This is described in Figure B.1. When the Majorana particles pairs up in the same site they are bound together and form ordinary fermions, in this case electrons. If the Majorana particles pair with particles in neighboring sites, this leaves two unpaired Majorana particles in both ends of the chain. These are spatially separated. The later pairing describes the topological superconductor phase [30].

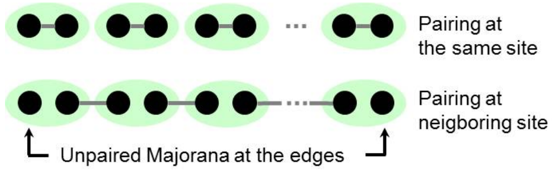

Figure B.1: The Kitaev chain describes two ways that the Majorana particles can pair up. In the upper chain Majorana particles in the same site pair up, bounding them to normal fermions. In the lower chain the Majorana particles pair up with another Majorana particle in a neighboring site. This leaves two unpaired spatially separated Majorana particles at the two ends of the chain. This describes the topological superconductor phase.

The topological superconducting state is highly delocalized. The Majorana particles are spatially separated but paired in a fermionic state. The state can be manipulated by physical non-abelian exchange physics, but is protected from most types of decoherence [28] and hence very interesting for future applications. The reason for the stable state is that local perturbations only has local effects and the paired Majorana particles are spatially separated.

The Kitaev chain exists in two realizations, based on semi-conducting quantum wires with strong spin-orbit coupling and based on 3D topological insulators such as Bi_2Te3 and Bi_2Se3 [16]. Superconductivity is induced through proximity effect with a conventional superconductor and a topological superconductor is established. Majorana particles are predicted to appear under the certain conditions as in these interfaces. The conditions are different for the quantum wire and the 3D topological insulator, due to the dimensionality of the quantum system.

C

Additionally conducted projects

C.1 Gating of the topological insulator

The surface of the topological insulators should be isolated from the bulk, which could be done by doping. Chemical doping has been done on Bi_2Se_3 where the bulk conductivity can be disregarded by electrolyte back gate doping [44]. Since Bi_2Te_3 and Bi_2Se_3 are more sensitive to applied fields than semi-conductors [11], their carrier density should be modified by electro-doping [45]. Electromagnetic field doping is of special interest since it is easy to tune and not permanent as chemical doping.

A separation of top and bottom surface conduction was recently demonstrated by Yu *et al* [37] with gate dependent Shubnikov-de Haas oscillations. Two types of oscillation behaviors were measured. When the gate voltage was swept only the top surface conduction was influenced, consequently one of the frequencies changed but the other one did not. Sweeping the gate also modified the type of charge carriers in the Bi_2Te_3 from n- to p-type.

Electromagnetic field doping was done as a side project early during this thesis, but was not successful. Three different designs were considered for the electro-gating; gating from the top, from the sides and from below. The top gate was put on top of the topological insulator flakes with an electrolyte as a spacer between. The coplanar gate was realized in the same fabrication step as the electrodes, with a distance of $2\,\mu$m from the flake and the electrolyte was put on top of the device seen in Figure C.1.

Both the top and coplanar gate seemed to influence the samples, but the effect could also have been due to the electrolyte reacting with the sample [46]. A clear drift in resistance was shown over the timescale of an hour. The bottom gate was realized, but required a lot of effort to place the flakes on top of the pre-patterned substrate. In addition, the precision of the electrodes had to be exact and could so far not be realized. This design should be further developed since it seems promising. However, the samples need to have low bulk conduction for continuation of the electromagnetic field doping. New experiments with coplanar gating could also be done, but then with purely electronic proximity gating.

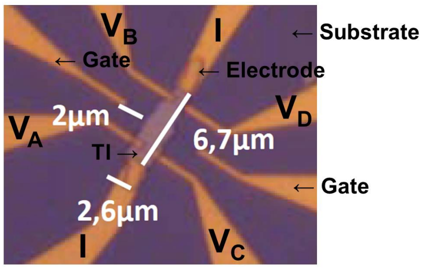

Figure C.1: Microscope picture of a Hall bar fabricated through exfoliation and electron beam lithography, together with electrodes for co-planar gating. The current was induced through the current electrodes, marked with I. The voltage could be measured either along the current channel (V_{AB} or V_{CD}) or transverse (V_{AC} or V_{BD}) at the same time as a potential difference was applied over the gate 2 μm from the flake.